Title: Efficient pheromone navigation via antagonistic detectors

Authors: Xuan Wan[1,2], Tingtao Zhou*[3,4], Vladislav Susoy*[5], Alessandro Groaz[1,2], Core Francisco Park[5], John F. Brady[3,4], Aravinthan D.T. Samuel[5], Paul W. Sternberg†[1,2].
*These authors contributed equally to this work.
† corresponding author

Author affiliations:

1. Division of Biology and Biological Engineering, California Institute of Technology, Pasadena, CA 91125, USA.
2. Tianqiao and Chrissy Chen Institute for Neuroscience, California Institute of Technology, Pasadena, CA 91125, USA.
3. Division of Engineering and Applied Science, California Institute of Technology, Pasadena, CA 91125, USA.
4. Division of Chemistry and Chemical Engineering, California Institute of Technology, Pasadena, CA 91125, USA.
5. Department of Physics and Center for Brain Science, Harvard University, Cambridge, MA, USA

Corresponding author: Paul W. Sternberg

Address: Tianqiao and Chrissy Chen Institute for Neuroscience, California Institute of Technology, Pasadena, CA 91125, USA.

Email: pws@caltech.edu

Author information:

Name	Email	ORCID
Xuan Wan	wanxuan@caltech.edu	0000-0002-6165-6340
Tingtao Zhou	tingtaoz@caltech.edu	0000-0002-1766-719X
Vladislav Susoy	vladislav_susoy@fas.harvard.edu	0000-0002-0669-0087
Alessandro Groaz	agroaz@caltech.edu	0000-0002-3873-7409
Core Francisco Park	corefranciscopark@g.harvard.edu	0000-0002-9542-2913
John F. Brady	jfbrady@caltech.edu	0000-0001-5817-9128
Aravinthan D.T. Samuel	samuel@g.harvard.edu	0000-0002-1672-8720
Paul W. Sternberg	pws@caltech.edu	0000-0002-7699-0173

Abstract

Chemotaxis to a moving potential mate emitting a volatile sex pheromone poses a navigation challenge that requires rapid, precise responses to maximize reproductive success. Volatile chemicals form gradients that differ from soluble compounds, potentially making navigation based on comparisons between spatially separated sensors unreliable for small-bodied animals. Contrary to this model of simple spatial comparison, *C. elegans* employs an antagonistic strategy, comparing inputs from head (AWA) and tail (PHD) sensory neurons with distinct response properties. Despite sharing a receptor, SRD-1, these detectors play different roles: AWA head neurons promote forward movement and acceleration, while tail PHD neurons induce reversals and deceleration. In increasing pheromone gradients AWA dominates; whereas decreasing gradients inactivate AWAs, allowing PHDs to fine-tune the response and correct the trajectory. Head AWAs are essential for mate-searching, while tail PHDs are crucial for complex tasks. Using a minimal-parameter computational model that recapitulates key findings, we infer

the interplay between head and tail signals in adaptive navigation. This study reveals a sexually dimorphic dual-detector system that integrates antagonistic sensory inputs from head and tail neurons to enable adaptive navigation strategies essential for efficient free-moving target location in dynamic environments.

Keywords: sensory integration, navigation, chemotaxis modeling, sex pheromone, sexual dimorphism

Introduction

For most animals, finding a mate is an essential task and is an especially significant challenge for organisms that rely on volatile pheromones for mate detection, as the potential mate often moves in a complex environment and establishes a fleeting, low concentration pheromone gradient. To obtain a mechanistic understanding of how animals can rise to this challenge, we studied navigation in *C. elegans* as it has a highly accessible nervous system.

Self-fertilizing *C. elegans* hermaphrodites emit a volatile pheromone when sperm are depleted [1-5]. Volatile chemosensory signals are fundamental to facilitating complex behaviors such as strategic navigation, active sampling, and sequential decision-making across diverse species; they are crucial for reproductive success [6-8]. As sex pheromones guide both innate and learned mate-searching activities in many animals, they provide an opportunity to study the neurobiological underpinnings of sexually dimorphic behaviors [9-18]. For example, the differential responses of males and females to identical stimuli, such as sex pheromones, raise questions about the sensory and neural circuit bases of sexual dimorphism in behavior [19-22].

C. elegans produces both soluble and volatile sex attractants. Soluble nematode-specific ascarosides are modulators of social/sexual behaviors and developmental regulation [23-41]. In contrast, this study focuses on a volatile, non-ascaroside sex pheromone (hereafter referred to as “the volatile sex pheromone”) that remains chemically unidentified but plays a critical role in sexual communication by signaling fertility and sexual maturity, as it can only be produced by hermaphrodites with no sperm due to depletion or dysfunction [3,42]. As hermaphrodites with no sperm can be considered females we classify this pheromone as a female sex pheromone. The only known receptor for volatile sex pheromone is the G protein-coupled receptor (GPCR) SRD-1, which is expressed in the sex-shared amphid neuron AWA in males only, implying underlying sexually dimorphic sensory processing by that neuron [4].

The complexity of neural circuit questions makes studies in simple models such as *C. elegans* highly useful to rigorously define neural algorithms used by animals. The neural circuitry underlying chemoattraction in *C. elegans* has been mapped with increasing precision, suggesting that sensory neurons process environmental stimuli with remarkable reliability [43]. Besides of the sensitive sensory neurons, it also has a network of interneurons that plays critical roles in processing sensory information and guiding behavioral responses that collectively facilitate navigation and avoidance behaviors: AIA amplifies olfactory signals, AIB controls reversals, AIY mediates response to gradients, AIZ modulates turns, and AVA initiates backward movement [44-52]. These circuits facilitate essential survival behaviors, employing mechanisms such as temporal integration [43], rapid desensitization [53], and the modulation of behavioral responses based on previous experiences and current conditions [44,48,54-65]. In short, the probabilistic nature of behavioral outcomes in *C. elegans* can be traced to the dynamic state of the neural network beyond sensory neurons, potentially explaining the variability in behavior outcomes from identical stimuli in the same individual [54,66].

Previous studies have shown that *C. elegans* employs sensory detectors on opposite ends of its body for rapid avoidance responses to aversive stimuli like SDS, H2O2, and glycerin [67-69], where quick response is prioritized over accuracy. In contrast, our study uncovers a novel volatile attractant chemotaxis mechanism in which dual detectors are instead used for target searching, a process that demands both rapid responses and high precision to successfully locate the target. Here, we describe a unique attractant dual-sampling algorithm that utilizes controlled expression of a single receptor to achieve sexually dimorphic chemosensory responses and an innate, adaptive navigation strategy for efficient volatile chemical chemotaxis.

In this study, we discover that the tail neuron, PHD, in addition to AWA, expresses SRD-1 and responds to the sex pheromone as well. We demonstrate that PHD is specifically required for navigation during challenging tasks. Using optogenetics, we compare the contributions of head and tail neurons to behavioral responses. To understand their interaction, we investigate the neural circuitry connecting them, and revisiting their response properties, we find that head and tail neurons detect distinct aspects of the pheromone gradient and concentration. Based on these findings, we propose a computational model to help elucidate navigation strategies.

Main

Volatile pheromone receptor SRD-1 is expressed in PHD, a male-specific neuron in the tail

Male *C. elegans* sense the volatile female sex pheromone via SRD-1 [4,42], a GPCR. In hermaphrodites, it is expressed only in ASIs in head region and PHAs in tail region. Whereas In males, SRD-1 is expressed in the AWA and ASI sensory neurons in head region. In males, SRD-1 was reported to be expressed in a pair of tail neurons [70,71], which we now have identified as the newly discovered pair of PHD neurons using several transcriptional reporters, based on their location, morphology, and marker gene expression (Figure 1A extrachromosomal array strain (*srd-1*p::mCherry),2A and S1B integrated cGAL-UAS strain (*srd-1*p::cGAL; UAS::GFP), and S1C marker for Ray B neurons cGAL-UAS strain *pkd-2*p::cGAL; UAS::GFP; *srd-1*p::mcherry). We further verified SRD-1 expression in PHD neurons using a split cGAL driver with *lin-48d* and *srd-1* promoter, where *lin-48* is known to be expressed in PHD neurons [72]. The expression of SRD-1 in PHD neurons was further supported by recent male-specific neuronal transcriptomics data, which revealed heterogeneous SRD-1 expression within these neurons [73]. Under normal conditions, only approximately 40% of PHD neurons express SRD-1 [73]. Our approach also generated a PHD-specific driver for targeted manipulation of PHD neurons for subsequent experiments (See Figure 2). In *C. elegans* males, AWA is required for chemotaxis towards the sex pheromone [4,42]. While previous studies have linked male tail-specific neuron PHD to various aspects of male behavior [72,74], their specific function remains unclear.

AWA neurons are known to respond to multiple volatile attractants [75-79], whereas PHA neurons are involved in repellent avoidance behaviors [67,76,80], and ASI mediates multiple sensory responses, including repulsion [81]. The sex-specific expression pattern of SRD-1 suggests that the differing behavioral responses to the sex pheromone—strong attraction in males and weak repulsion in hermaphrodites—may result from the sexually dimorphic expression of the chemoreceptor SRD-1. Additionally, the dual-site expression of SRD-1 in both head and tail neurons suggests that males may integrate SRD-1-mediated sensory inputs from the anterior and posterior regions to navigate effectively toward the volatile pheromone.

Male-specific PHD is activated by the volatile pheromone

We next tested if PHD neurons activate in response to the sex pheromone (Figures 1C). We observed that PHD is activated by the sex pheromone from both *C. elegans fog-2* hermaphrodites and *C. remanei* females. To test if this response was mediated via SRD-1, we repeated the experiment in *srd-1(eh1)* loss-of-function mutant males. *srd-1* mutant males showed no PHD activation upon sex pheromone stimulation (Figure 1C). Therefore, male-specific PHD neurons sense volatile sex pheromone via SRD-1. These findings, combined with the known role of PHD in mate-related behaviors [72], suggest its potential involvement in pheromone-guided navigation. Calcium imaging demonstrates that SRD-1 expression in both head (AWA) and tail (PHD) neurons is not merely anatomical but functionally mediates pheromone responses, providing direct evidence that males employ dual detectors to sense pheromone sources.

PHD neurons enhance mate-searching efficiency in complex environments

To test the hypothesis that these spatially separated detectors for pheromone actually aid navigation, we used four types of chemoattraction assays designed to represent varying levels of difficulty males might encounter in natural conditions, comparing intact males to those with HisCl inhibited-PHD neurons (Figure 2). We achieved specific expression of the HisCl effector (a chemogenetic silencer) in PHD under the control of a split cGAL-UAS line: *lin-48d*p::NLS::cGAL (DBD); *srd-1*p::NLS::cGAL (AD) (Figure 2A), and our experimental design included wild-type males and PHD-HisCl lines without histamine treatment as controls. Our data showed no significant differences between the two control groups in their response to sex pheromones under all test conditions (Figure 2C-G). Therefore, any observed effects can be attributed to the treatment-induced inactivation of PHD neurons.

We first challenged PHD-inhibited males to locate a sex pheromone source placed at the same distance (3 cm) from the source, using two different diameters (6 and 8 cm)agar-filled Petri dishes (Figure 2C, D). All males located the source within 30 mins. PHD-inhibited males performed as effectively as controls at both distances, indicating that tail neuron input is not essential for simple, close-range navigation tasks. By contrast, when we increased the distance and placed males 5 cm from the source in an 8 cm-Petri dish (Figure 2E), all test subgroup males were unable to locate the source.

We then tested males' ability to locate a more dilute odor. We diluted the sex pheromone concentration 10-fold and observed the responses of both wild-type, HisCl-untreated control, and PHD-inhibited males (Figure 2F, S2A). PHD-inhibited males exhibited notable difficulties in identifying the diluted pheromone source, unlike the two control group males. This differential response underscores the essential role of male tail PHD neurons in navigating toward weak pheromone signals.

To understand the effects of increased distance versus stimulus dilution, we conducted Finite Element Simulations of the pheromone concentration field (Figure S3). In our assay setup, the stimulus was placed on the lid of the plate that was half-filled with agar, creating a bi-layer distribution of the pheromone. As illustrated in Figure S3A, the volatile component diffuses rapidly in the air, while the agar absorbs and then slowly releases the volatile component. The concentration field simulation revealed that in experiments where males were positioned far away from the pheromone source, they encountered areas of low absolute concentration without a clear gradient. Conversely, when males were tested nearer to a diluted pheromone source (3 cm), their performance, while reduced relative to controls, was better than in the 5 cm experiment, likely because the diluted source still produced a weak but discernible Gaussian gradient despite its overall low concentration (Figure S3B). These findings suggest that the concentration gradient plays a crucial role in guiding males to the pheromone source.

Since *C. elegans* navigate through three-dimensional (3D) soil and rotting fruit in their natural habitat, we examined the efficacy of PHD-inhibited males in a 3D search paradigm using gellan gum gel (see

Methods), which likely better mimics natural conditions than a 2D Petri dish surface (Figure 2G, H). In this endpoint assay, we recorded the number of worms that reach the target spot every 5 minutes. Worms must stop moving at the exact 3D location (depth included) of the pheromone to count as finding it. Control and test droplets are placed at the same depth to control for vertical bias, avoiding confounding from a preference for movement toward the surface or bottom. PHD-inhibited males had reduced proficiency in identifying pheromone sources within 3D spaces, underscoring the importance of PHD neuron inputs for environmental navigation that mirrors natural conditions (Figure 2G, S2A).

Analysis of the distribution of males at multiple timepoints after the addition of stimulus revealed a uniformly low chemotaxis index for the PHD-inhibited male group across all intervals in weak signal and 3D exploration tasks (Figure S2B). In our 2D experiments involving weak signals, most control males successfully located the target within 10 minutes. However, in 3D exploration tasks, the peak arrival time at the target extended to a significantly longer 20 minutes (Figure S2C). Notably, we observed distinct impairments in the navigational behaviors of PHD-inhibited males between weak signal detection and 3D spatial exploration tasks. In weak signal detection, the low chemotaxis index resulted from an equal distribution of males reaching both the test and control spots. Conversely, in 3D searching tasks, the low chemotaxis index stemmed from fewer males reaching both spots (Figure S2B-D).

Optogenetic dissection of SRD-1 positive neurons and PHD neuron's roles in male locomotion

To examine the effects of head versus tail SRD-1 positive neurons on sex pheromone-induced behavior, we used the red-shifted Chrimson variant of channelrhodopsin [82]. We first evaluated the UAS::Chrimson effector driven by a pan-neuronal promoter, demonstrating the system's efficacy (Figure S4A): worms temporarily ceased movement during light stimulation, promptly resuming normal behavior once the light was switched off.

We then activated all SRD-1 positive neurons with Chrimson expressed under the *srd-1* regulatory control, using an *srd-1*p cGAL driver (Figures 3A ATR- and S4C ATR+). The absence of ATR served as a control to negate any potential effects of light alone, confirming that the observed changes in velocity were attributable from targeted neuron activation. Under ATR+ conditions (Figure 3A), males exhibited continuous forward movement throughout the 12.5s light stimulation period, transitioning to rapid steering or reduced speed after stimulation ceased, but not in ATR- males (Figure S4C).

To further confirm the role of SRD-1-positive neuron stimulation in modulating locomotor behaviors, we investigated the effects using extended stimulation protocols (30s or 60s light-on intervals followed by 10s light-off intervals) (Figure 3C). During prolonged stimulation, forward movement was sustained, while turning behaviors remained consistently suppressed. Also, the cessation of stimulation was associated with reduced movement speed and an increase in turning rate, consistent with observed dynamics under shorter stimulation conditions. Using the *odr-10*p cGAL driver to activate AWA neurons in both sexes showed no behavioral change, suggesting AWA activation alone does not drive forward motion, or the *odr-10* promoter provides insufficient expression levels (Figure S4B).

We next targeted PHD neurons exclusively. Using a split cGAL driver under the control of *lin-48d* and *srd-1* promoters, we achieved PHD-specific Chrimson expression (Figures 3B ATR+ and S4D ATR-). Under the ATR+ condition, PHD activation in males elicited a decline in average velocity throughout the red light stimulation period, after which males resumed movement. However, this was not observed in ATR- males. This result contrasts with the overall movement patterns observed upon and after the activation of all SRD-1 positive neurons (See Figure 3A). Previous studies also suggest that PHD neurons have a potential role in maintenance of backward locomotion during the mating partner body scanning [72]. We

also observed that repeated activation of PHD neurons also resulted in a gradual reduction in velocity (See Figure 3B right panel), suggesting a persistent slowdown effect on locomotor behavior after activation.

Since we also observed behavioral responses to light stimulation in hermaphrodites, we performed a quantitative analysis to distinguish the robustness of these responses in hermaphrodites and males (Figure 3). Hermaphrodite responses were more variable, as also seen in the average velocity (Figure 3c) and Fourier analyses (Figure 3d). Fourier analysis of total velocity during SRD-1-positive PHD neuron stimulation revealed prominent peaks at 0.05 Hz and 0.025 Hz, corresponding to the 20 s and 40 s stimulation protocols, respectively (Figure 3d). The amplitude and sharpness of the spectral peak at 0.05 Hz (or 0.025 Hz) quantifies the strength of the signal, i.e., the consistency and robustness of the behavioral response to periodic stimulation, and it is consistently stronger in the males' response than the hermaphrodites' by about a factor of two. Hence, we concluded that males display a more robust response. The more variable response in hermaphrodites also manifested as larger inter-individual differences, as shown by comparing the error bars (shaded area) in Figure 3c in the left two panels. Both these analyses suggest a sex-specific effect of SRD-1-positive neuron activation. Upon PHD neuron stimulation, the male also showed a large error bar. Recent male neuron transcriptomics data from the Murphy group revealed that only ~40% of PHD neurons express SRD-1 under normal conditions [73], and this partial penetrance of SRD-1 expression could explain the behavioral variability we observe in males, as individual worms would differ in their functional PHD neuron complement.

Head and tail neurons mediate distinct micro-behavioral responses to optogenetic activation

To confirm and further investigate how activation of SRD-1 positive neurons in the head versus the tail affects behavior, we optically targeted either the head or tail of freely moving males expressing *srd-1* Chrimson cGAL-UAS.

Initial observations showed that males predominantly moved forward in the absence of stimulation (ATR– controls, Figure 4, S4 and S5), so a short observation window could lead to a false positive result on forward movement. To evaluate the duration and persistence of this response, red light is applied to head region for 30s (Figures 4A). As shown in Figure 3, tail stimulation primarily induced reversals, a rapid transition from forward to backward movement. For the tail region stimulation, we chose short and repeated pulses alternating every 2s over a 15-cycle period to capture multiple reversals (Figure 4A).

After postprocessing, we divided the recording into 2-second segments. For each 2-second segment, we tabulated the behavioral motif displayed by the male or the first behavioral transition that occurred during that segment. We used two complementary behavioral classification frameworks to capture distinct aspects of locomotion dynamics. : Four-Motif Analysis (Figure S5): Focuses on core locomotion states (forward, backward, forward-to-backward transition, backward-to-forward transition) to highlight macro-level movement changes during head/tail stimulation. Six-Motif Analysis (Figure 4): Expands categorization to include nuanced behaviors like self-exploratory (where the worm attempts to probe its own body) and hesitation (marked by frequent direction changes within the 2-second window), which better capture micro-behavioral variability.

A short light pulse delivered to the tail region induced a transition from forward to backward movement, accompanied by increased directional hesitation (Figure 4B). During these hesitant periods, males frequently switched between forward and backward locomotion. However, we observed substantial individual variability in response to tail stimulation. While most worms reliably responded to light stimulation and for 7 pulses, they responded an average of 4.3 times. A subset completely ignored the

stimulus. This behavioral heterogeneity may arise from the variable expression of SRD-1 in PHD neurons [73].

With 30 seconds of head stimulation, we noted behaviors analogous to those from activating all SRD-1 positive neurons, including persistent forward movement during light exposure followed by rapid directional adjustment (Figures 4C, S5C). We also observed that after head stimulation, males exhibited self-exploratory behavior (Figure 4C), using their tails to probe against their bodies, a behavior that can persist for several minutes.

Circuit that combines head and tail inputs to control locomotion direction

The male connectome [83] suggests locomotion command neurons are the likely locus of integration of the head and tail inputs. Specifically, PHDs have strong connections to PVN (ROI1) and EF (ROI2) interneurons [83] (See Figure 1B), which connect to pre-motor command neurons. The direction of locomotion is controlled by reciprocal inhibition of forward and reverse command neurons [44,50,84,85]. To investigate the circuitry between sex pheromone sensory neurons and these motor command neurons, we specifically activated SRD-1 positive neurons with Chrimson and monitored pan-neuronal calcium dynamics using GCaMP6s (Figure 5A-C, see Method). SRD-1 positive neurons, including PHD, AWA, and ASI neurons in males, had robust responses to light stimulation (Figure 5C). In addition, two groups of neurons within the male tail region—presumably a pair of PVN neurons in one region of interest (ROI1) and a single EF neuron in ROI2 (Figure 5B-C, S6)—had a strong positive correlation with PHD activity in ATR+ and not in ATR- males (Figures S7). Here, we used normalized activity for regions of interest (ROIs) to facilitate comparison across populations of neurons with varying baseline fluorescence, while raw activity was analyzed for single neurons to preserve their intrinsic activity dynamics and avoid potential distortions from normalization. In the male head region, we observed a more negative correlation with light stimulation. About 4 neurons in the head region are positively correlated with AWA neuron activity and about 10 neurons are negatively correlated (Figure S7).

We observed a strong negative correlation between the activity of the reversal command neurons (AVA) and SRD-1-positive neurons in the head region (AWA and ASI). Although this inverse relationship was also present in the ATR-untreated control group, it was less pronounced. In ATR-untreated worms, the decrease in AVA activity may have been influenced by factors such as movement of the microscope objective or non-specific light responses.

AWA and PHD have distinct response properties

It has been suggested that AWA neurons adjust their response based on fold-changes in odor concentration, reducing turning behavior with minimal increases in odor concentration [53]. We used prolonged, behaviorally relevant high concentration sex pheromone stimulation with a thin layer micro-diffusion (TLMD) unit (Figure S8A, see Method), facilitating pan-neuronal calcium imaging (Figure 5D and E) [4]. As shown in Figure 5D, upon pheromone application, AWA and ASI neurons showed immediate calcium influx followed by rapid desensitization to a low, steady state within 1.5 mins, maintaining this level for at least 5 mins. This pattern indicates robust desensitization to even relatively high pheromone concentration. PHD neurons exhibited sustained activation for at least 9.5 mins with a gradual decline, indicative of their threshold-sensing properties (Figure 5E). 62.5% of imaged males exhibited a rapid response to pheromone exposure and sustained high levels of activity, whereas the remainder displayed a slow response, with delayed activation (2.5 mins post-stimulus) with a 40% reduced calcium signal amplitude (Figure 5E, cropped to 250 second; D, full length 600 second). The fast and slow responses of PHD neurons are particularly intriguing. Recent male neuron transcriptomics data revealed a heterogenetic expression of SRD-1 in male PHD neurons, which may result in this individual variation.

322 This pattern may also be caused by PHDs being actively inhibited by other neurons. According to the
323 connectome, PHDs are post-synaptic to several neurons [83], which may modulate their activity and
324 contribute to the observed variability in response dynamics.
325
326 During the initial phase of neuronal activity, before the activation of PHD neurons, pheromone-
327 stimulated calcium imaging revealed a negative correlation between reversal command neurons (AVA
328 and AVE) and head sensory neuron activities (AWA and ASI) (Figure 5D). This negative correlation
329 suggests that the inhibition of reversal command neurons by head neurons is pivotal for forward
330 movement during gradient ascent. As demonstrated by the set of optogenetic experiments (see Figure 3
331 and 4), gradient-sensing neurons in the head region dominate PHD input and primarily drive forward
332 movement, suggesting that head neuron activity may override tail neuron activity.
333
334 In the subsequent phase of neuronal activity, AWA and ASI activity became hyperpolarized, and all PHD
335 neurons were activated. This allowed us to examine the direct correlation between PHD neurons and
336 reversal command neurons (AVA and AVE). We observed that reversal command neurons exhibited a
337 negative correlation with head sensory neurons and a positive correlation with tail sensory neurons
338 (PHD) (Figure 5F), suggesting PHD-mediated activation of reversal command neurons, consistent with
339 the observed reversal behavior during optogenetic activation (see Figures 3, 4).
340
341 **PHD and AWA neurons drive AVA activity at distinct concentration thresholds**
342
343 To confirm the correlation between reversal command neurons and anterior and posterior SRD-1-
344 positive neurons in different sex pheromone concentrations, and to determine the concentration
345 threshold for behavior changes, we fabricated a head and tail multi-inlet microfluidic chip (Figure 6A).
346 We utilized immobilized worms within microfluidic chips to precisely control the delivery of varying
347 concentration stimulations to the head or tail independently. This setup enabled accurate stimulus
348 application to distinct regions and facilitates switching between a control buffer and three different
349 stimulus concentrations.
350
351 *C. elegans* has five pairs of premotor command interneurons, two of which promote forward locomotion
352 and three of which promote reverse locomotion. These groups are interconnected and control distinct
353 motor neurons [44,50,84,85]. AVA neuron activity peaks at the start of a reorientation [44,49,50,52,84] and AVA
354 interneurons integrate opposing signals from head and tail sensory neurons, guiding behavior [68,86]. AVA's
355 diverse activities across time scales position it as a key neuron in coordinating forward and backward
356 movements [68,86]. Therefore, monitoring AVA neuron activity provides a useful indicator of the animal's
357 forward and reversal behaviors.
358
359 Using diacetyl as a baseline attractant to validate our device (Figure 6B-b), we observed that all tested
360 concentrations led to decreased AVA neuron activity, suggesting an enhancement of forward movement.
361 Diacetyl at higher concentrations more effectively suppresses AVA neuron activity. We then tested
362 pheromones at varying concentrations applied to both ends and separately to the head and tail (Figure
363 6B-c). Simultaneous stimulus of both ends immediately decreased AVA activity, indicating forward
364 movement. Remarkably, head-only stimulation caused a greater reduction in AVA activity compared with
365 stimuli to both ends, whereas tail-only stimulation resulted in increased AVA activity (Figure 6B-d,e); this
366 difference suggests antagonism of head and tail input, consistent with our optogenetic and sex
367 pheromone stimulation calcium imaging showing that head neurons activation promotes forward
368 movement and tail PHD neuron activation triggers reversal (see Figures 3, 4 and 6Ba). These increases
369 and decreases in AVA activity only last for one minute.

We performed area-under-curve (AUC) analysis on the AVA neural activity data (See Method). Notably, SRD-1 positive neurons in the head and tail show different preferences for sex pheromone concentrations. Higher pheromone concentrations more effectively suppress AVA activity when applied to both ends or exclusively to the head (Figure 6Bc-d). In contrast, AVA activation peaked at pheromone dilutions of 100–500X when applied only to the tail (Figure 6C). But, at dilutions of 500X, 1000X, and 2000X, AVA neurons displayed predominantly random oscillations when pheromones were applied to the head or both ends (Figure S10D). These findings suggest that higher pheromone concentrations promote forward movement more effectively, with head neurons strongly inhibiting AVA activity and weaker tail neuron activation contributing to sustained forward movement and increased speed. At low concentrations, the inhibition from head neurons diminishes, and tail neuron activation becomes more prominent, reducing forward movement. We also noted significant spontaneous oscillations in AVA neuron signals across individuals, a finding shown in similar studies using microfluidic chips [66,87,88]. These fluctuations are likely due to the inherent spontaneous oscillation nature of AVA neurons, individual animals' internal status, and the restrictive environment of the microfluidic channels, which may discomfort the worms and trigger attempts to escape, causing variable AVA neuron signal patterns.

Command neurons integrate antagonistic inputs from the head and tail

The integration of inputs from SRD-1-positive neurons in the head and tail regions reveals a sophisticated signal-processing algorithm that optimizes navigation. Optogenetic stimulation data (Figures 3, 4) demonstrate that activation of tail-region neurons induces reversal behavior and slows locomotion, while stimulation of head-region neurons suppresses turning, promotes forward locomotion, and increases speed. Notably, head-region activation alone mimics the effects of activating all SRD-1-positive neurons, highlighting the dominant role of anterior SRD-1-positive neurons in guiding behavior. This aligns with findings from AWA-defective *odr-7* mutants and AWA laser-ablated males [4,42], where AWA neurons are critical for locating pheromone sources, while ASI and PHD neurons are insufficient on their own. Conversely, the absence of tail-region PHD neurons impairs pheromone localization under natural, complex conditions, though it has minimal effects in ideal laboratory settings with high pheromone concentrations, reduced noise, and simpler navigation challenges (Figure 2C, D). Together, these data suggest a dual-detector system in males integrating head and tail neurons' sensory input, with tail neuron activation acting as a corrective mechanism during navigational errors to enhance chemotaxis efficiency.

Pheromone stimulation calcium imaging data further elucidates this integration (Figure 5D). By fitting AVA neuronal activity into a linear model incorporating AWA and PHD activity, the best-fit equation has AVA activity = −0.7 × AWA activity + 0.1 × PHD activity − 0.2, indicating that AVA responses are primarily driven by inhibitory input from AWA neurons in the head, with a smaller excitatory contribution from PHD neurons in the tail (Figure 5F).

Microfluidics chip-based experiments (Figure 6D) further validated this integration mechanism. The area under the curve (AUC) of AVA neuron activation during head-specific and tail-specific stimulation closely matches the trends observed with dual stimulation. This suggests that the neuronal response results from a combination of antagonistic inputs from head and tail regions, providing a computational framework for navigating pheromone gradients. This dual-system integration reflects a sex-specific chemoreceptor-driven behavioral adaptation for efficient navigation in complex environments.

A simple computational model for spatially separated detectors navigation in *C. elegans*

Sensory neuron inputs are typically conserved through the connectome and determine the behavioral outcomes [53]. Summarizing the experimental observations of the strong correlations between the AWA, PHD and AVA neurons (Figures 5, 6), we propose a simple model to demonstrate the roles of head and tail sensory inputs. We focused on macroscopic navigation behavior and neglected details of microscopic traits and changes in worm body curvature in motion.

C. elegans exhibits a remarkable ability to navigate complex environments using chemical cues. Two established directional navigation strategies have been observed [76,89-94]: (1) Klinokinesis, a random walk biased toward the stimulus, such as in bacterial chemotaxis, requires comparing concentrations over time to adjust random turning that lacks directionality towards the correct heading. (2) Klinotaxis, a more refined navigation, utilizes directional turns to achieve more accurate gradient navigation [89,95-98]. Here, we modeled kinesis and taxis separately.

During kinesis searching, we modeled locomotion as a mixture of active Brownian motion [99] and run-and-tumble motion [100] (see Methods). Our first key assumption is that sensory inputs from the head and tail are converted into confidence variables Q^H and Q^T, which then determine the worm's dynamical state (Figure 7A). As the activity of reversal command neurons AVA and AVE is found to correlate negatively with AWA activation but positively with PHD neuron activation, we propose a simple form to qualitatively capture these correlations:

$$\gamma = \gamma_0 e^{-\lambda_K (Q^H - Q^T)},\ U = U_0 + U_1 (Q^H - Q^T + \eta).$$

Here $\gamma_0 = 0.067/s$ is the baseline tumbling rate. $U_0 = 0.064$ mm/s is the baseline average speed, and $U_1 = 0.03$ mm/s is the magnitude of speed fluctuation. λ_K represents the strength of klinokinesis, and η represents a Gaussian noise in the velocity. The worm's dynamic state is characterized by its velocity and tumble rate (U, γ). Loss of AWA or PHD input disrupts Q^H or Q^T computation, leading to impaired speed and turning regulation. The equations for (U, γ) connect the non-directional kinesis movements to confidence variables from head and tail inputs, which are subcircuit responses to stimuli on the head and tail sensory neurons. These mechanisms are also known as orthokinesis (for U) and klinokinesis (for γ).

Our model is based on the idea that sensory information coming from the worm's head and tail is translated into a signal that is a measure of 'confidence' (Q), and these signals directly determine the worm's behavior and movements (Figure 7A). AWA neurons become more active as sex pheromone concentration increases [4]. In our microfluidics chip-based experiment, we found that input from head neurons suppressed AVA neuron activity (Figures 5, 6B-d). Therefore, in our model, the confidence signal based on head input (Q^H) will rise with increasing pheromone concentration until it reaches saturation (see blue line in Figure 7A). Interestingly, high pheromone concentrations applied to the tail suppress AVA neuron activity, in contrast to the activation observed at low concentrations (Figures 5, 6B-e). Furthermore, continuous activation of the PHD neuron will result in a reduction in baseline velocity and the sprint behavior exhibited upon proximity to the target, suggesting that Q^T should decrease below zero to capture these observations (see red line in Figure 7A). We propose using the $Q^H - Q^T$ model (see purple line in Figure 7A) to represent the negative correlation between AVA/AVE command neurons and AWA activation, and the positive correlation with PHD neuron activation. Importantly, only $Q^H - Q^T$ accurately captures the observed increase in speed towards the end of navigation, which wouldn't be captured by simply adding the two signals together (compare purple and green lines in Figure 7A).

To determine the dynamics of Q^H and Q^T given external concentration field evolution, we adopt the simplest dynamics model with a single memory timescale:

$$\frac{dQ^H}{dt} = -k_1 Q^H + k_2^H f_H\left(C, \frac{dC}{dt}\right),$$
$$\frac{dQ^T}{dt} = -k_1 Q^T + k_2^T f_T(C).$$

Here $\frac{1}{k_1}$ is the timescale of memory, while the values of $k_2^{H,T}$ represent the sensitivity of SRD-1 positive neurons. f_H and f_T represent the sensory inputs, and they are chosen to qualitatively reflect the observations in this work and AWA calcium dynamics in [53] (see Methods). Key assumptions are: (1) the long decay time of PHD activity level during constant sex pheromone stimulation, as seen in Figure 5F, indicates that PHD sensory input mainly depends on the absolute concentration. Hence, f_T is only a function of C. (2) PHD response is positive at intermediate concentration ranges but becomes strongly suppressed at high concentrations, as shown in Figure 6C. (3) The relatively short decay time of AWA activity level during constant stimulation, as shown in Figure 2 of ref [53], indicates that AWA sensory response mainly reflects the detected concentration change, with a mild increase as absolute concentration increases. For simplicity, in this model worms will make directional (taxis) turns when they (1) detect a high enough concentration above a threshold value, and (2) if they currently experience a decrease in concentration. Such turns are assumed to be perfectly accurate toward the source direction. Based on our experimental observations, head-inhibited worms will not perform taxis turns.

We performed simulations for navigation on a small Petri dish with the concentration simulation for 30 mins (Figure 7B). Each simulation contains 10000 worms, initialized with random orientations. When both head and tail sensory inputs are missing, $Q^H = Q^T = 0$, the worms perform a standard active random walk with constant mean velocity and tumble rate (Figure 7C). Only a small fraction – about 10% of worms – were able to find the pheromone source by luck, as seen in the grey curve of Figure 7D and SI video S2.

Adding tail sensory input alone significantly enhanced the chance of finding the pheromone source, almost doubling the probability (Figure 7D light blue curve). Adding head sensory input boosts the overall success rate to nearly 100%, simply due to the dominating effect of taxis turns (SI video S1). Overall, with tail input, the trajectories are biased closer to the pheromone source, as shown in Figure 7E and S11. In each simulation, worms start from a small region around the center of the plate and the pheromone source is located at the red point on the left side. We denote the direction from the pheromone source to the plate center as the x direction and measured the average x position of all worms during the entire simulation. This is denoted as <x> on top of each panel in Figure 7E. We notice that <x> is negative whenever tail input is present but becomes positive when tail input is absent. Hence, tail input enables worms to move on average to the left side of the plate, i.e., they behave more attracted to the pheromone source with tail inputs. We compute the maximum distance from the pheromone source that reaches worm reaches during the search, denoted as d_{max}. For successful worms with head inputs, the addition of tail input accelerates their search so that their d_{max} is slightly smaller compared with those without tails. In the absence of either head or tail inputs, worms only perform random walks and stay near the starting position; adding tail input effectively incentivizes them to explore larger areas and be more biased to the source, manifested in significantly larger d_{max} values. Overall, these simulations suggest that tail input significantly improves the success rate of mate-searching.

Discussion

Computational modeling suggests tail input suppresses mistakes

Building on our computational modeling of pheromone diffusion, we find that tail input is essential for suppressing navigation errors arising from the rapid diffusion of volatile attractants. Specifically, our finite element method (FEM) simulations reveal that the pheromone concentration field deviates from Gaussian

distributions, and based on our simulations of the dynamical model, the resulting pheromone distributions can lead to artificial increases in head confidence Q^H for worms in low concentration regions due to the finite plate size, leading to erroneous behaviors without tail input. Compared to water-soluble chemicals studied previously, air-borne pheromones diffuse rapidly, creating a nonlinear process where the agar initially absorbs pheromones to a high concentration before emitting them back into the air. This non-Gaussian behavior is characteristic of chemicals transported across air and agar phases and must be considered in chemotaxis models.

The errors caused by artificial increase in head confidence can be mitigated by the tail. Tail input corrects these errors by increasing the tumble rate, ensuring more efficient directional adjustments. Moreover, suppressing PHD activity at high concentrations $Q^T \to -1$ significantly improves navigation, supported by GCaMP data showing reduced PHD activity under 1x concentration stimulation (Figure 4). Consequently, we adopted a functional form for PHD response: $\lim_{C\to 0} Q^T \to 0$, $\lim_{C\to C_0} Q^T \to 1$, and $\lim_{C\to \infty} Q^T \to -1$. These dynamic properties suggest that the interplay between head and tail neurons is critical for robust navigation strategies, offering an extensible framework for modeling chemotaxis in complex environments.

Critically, our simulations also revealed that the concentration differences between anterior and posterior positions are negligible due to the small size of the worms. This fundamental constraint necessitates an alternative navigation strategy: rather than measuring spatial differences along the body axis, *C. elegans* employs antagonistic comparison between functionally specialized head (AWA) and tail (PHD) neurons. This computational innovation allows robust navigation where traditional gradient sensing would fail.

Sexually dimorphic decision-making in *C. elegans* stems from sensory neuron inputs

The distinct responses of males and females to the same sex pheromone prompt questions about the neural foundations of behavioral sexual dimorphism [3,4,42]. Our findings indicate that sexual dimorphism in naïve *C. elegans* males' response to sex pheromone stimulation stems from variations in receptor expression. This leads to differential sensory neuron activity propagating through neural circuits, culminating in distinct behaviors. Although existing data from other organisms suggest that sex-specific pheromone responses arise from sexually dimorphic neural circuits rather than differential sensory perception [9,101,102], incomplete characterizations of neural networks in more complex model organisms may bias our interpretation of this phenomenon. *C. elegans* exemplifies an olfactory system where sophisticated modulation of a single receptor's expression allows both efficient chemotaxis and the execution of distinct sex-specific behaviors. Therefore, the behavioral outcomes in naïve animal during navigation can be predicted from activity of the key sex pheromone sensory neurons.

Decision in uncertainty: how worms navigate complex gradients with imperfect sensory input and inaccurate steering angle control

As a complementary approach to experimental observations of the worms' turning behaviors, we conducted mathematical analysis for the optimal turn angle and compared it for consistency with our observed data. We modeled an idealized worm with precise short-term memory of its trajectory and the ability to precisely detect concentration gradients in its path by traveling along the same direction for a short duration. We assume that the ideal worm's sensory systems are infallible and the worm's neural circuitry can process this information, such that sampling along two distinct directions will be theoretically sufficient to identify the gradient's direction. In practice, however, a non-ideal worm's memory and sensory perception are inaccurate due to inherent noise, complicating the task of gradient estimation. This

challenge mirrors a regression problem where the objective is to select an optimal turning angle for a second sample that minimizes the uncertainty in determining the gradient's direction. We assumed a steady concentration field that does not vary with time during the sampling of two directions of a non-ideal worm.

Our analysis for a non-ideal worm, grounded in a least-squared-error regression framework, suggests that the optimal choice for a second sampling direction consistently exceeds 90 degrees regardless of the initial sampling orientation relative to the actual gradient direction. With an initial orientation distributed uniformly randomly, the preferable turning angle is approximately 120 degrees (Figure S12). This direction is chosen to be away from the gradient if the initial angle is qualitatively aligned (less than 90 degrees from the gradient) and towards the gradient otherwise. Given the worm's lack of precise knowledge of gradient direction, it faces a choice: turn 120 degrees in either direction or, as a compromise, nearly 180 degrees (Figure S12). Observations suggest that worms likely opt for turns close to 180 degrees in early search stages, indicating a strategic approach to maximize information gain about the gradient's direction. Worms thus intricately balance their behavioral strategies with their sensation, motor control, and cognitive limitations.

A navigation strategy based on an integrative dual-detector mechanism

Dual detectors to control directional movement allow simultaneous comparison of stimulus rather than a single organ comparison in time. In *C. elegans*, the phasmid neurons in the tail, similar to the amphid chemosensory organs in the head, perform a chemosensory function [67]. Indeed, amphid and phasmid neurons influence the worm's backward movements when exposed to repellents, integrating sensory inputs from both the head and tail to promote effective escape behaviors [67,69,103]. The AVA interneurons consolidate signals from the head and tail sensory neurons to steer behavioral choices [103]. Our study provides the first evidence of dual detectors in attractant navigation. Repellents demand rapid avoidance (reversal), while attractant sensing requires complex, targeted navigation strategies.

For repellent avoidance behaviors, worms employ a simple strategy in which both head and tail inputs trigger reversal [67,69,103], distinguishing it from the more complex mechanisms underlying attractant navigation. In attractant navigation, head- and tail- located neurons utilize the same receptor but drive distinct and opposing sensorimotor responses: 1) AWA promotes forward movement and speeding up while PHD induces reverse movement and slowing down. 2) Behavioral output is typically dominated by AWA activation, while PHD input provides antagonistic modulation of AWA-driven behavior. 3) The head neuron exhibits gradient-sensing properties and rapid desensitization in constant concentrations, while the tail neuron displays threshold-sensing properties and remains activated under constant concentrations. 4) PHD neurons are activated at lower pheromone concentration, thus preventing males from making false taxis turns induced by rapid temporal evolution of volatile pheromone concentration. PHD neurons are inactive at high pheromone concentration, promoting rapid acceleration (sprints) as the male approaches the pheromone source. We computationally modeled the response, proposing that males have a measure of confidence that they are proceeding in the right direction; the absence of PHD input disrupts directional confidence, preventing the acceleration response. This demonstrates a fundamental aspect of neural circuitry: different neurons have evolved to handle distinct environmental stimuli.

Contrary to prior hypotheses [104-107], *C. elegans* does not rely solely on simple head-tail concentration comparisons but instead employs a more complex antagonistic mechanism involving head and tail sensory neurons, each with distinct preferred concentrations for optimal activation. Our proposed mechanism focuses not on the spatial separation of receptors but on comparing signals from two distinct sensory neuron types, AWA and PHD, with different response properties. This comparison enables the animal to integrate various aspects of pheromone gradient dynamics and make adaptive behavioral decisions. While

604 the mechanism relies on comparing outputs from these neurons, their differences stem more from their
605 response characteristics rather than their physical locations. This strategy would be particularly beneficial
606 for navigating a volatile gradient, such as a shallow and low-concentration pheromone gradient, where
607 there is minimal difference in concentration between the worm's head and tail, making head-tail absolute
608 concentration comparisons very unreliable.
609
610 Besides our work, other studies have shown that numerous chemosensory GPCRs are also co-expressed
611 in the head amphid and tail phasmid neuron classes [67,108-111], which raises the possibility that this
612 antagonistic detector mechanism may represent a general strategy in *C. elegans* navigation. This
613 mechanism, integrating distinct neuronal responses to environmental stimuli, allows precise adaptation
614 to dynamic and complex sensory landscapes. Beyond pheromone navigation, the principles uncovered
615 here likely extend to other volatile chemosensory contexts, providing a broader framework for
616 understanding how animals solve the universal challenge of searching for moving targets within noisy and
617 variable environments.
618
619 **STAR Methods**

620 **Key Resource Table**

REAGENT or RESOURCE	SOURCE	IDENTIFIER
Bacterial and virus strains		
E. coli	*Caenorhabditis* Genetics Center (CGC)	WormBase: OP50; WormBase: WBStrain00041969
Experimental models: Organisms/strains		
him-5 (e1490) V	CGC	CB4088 (male enriched mutant)
srd-1(eh1)	CGC	CB5414 (*srd-1* mutant)
syEx1972 [srd-1P::mCherry]; syEx1974 [unc-119::gfp]	This study	PS10451 (*srd-1* reporter; pan-neural marker)
syEx1973 [rab-3P::mCherry]; syIs912[srd-1P::Gal4(sk)::VP64]; syIs300 [15xUAS::GFP]	This study	PS10448 (*srd-1* driver; GFP effector; pan-neural marker)
syEx1972 [srd-1P::mCherry]; syIs913 [pkd-2P::Gal4(sk)::VP64]; syIs300 [15xUAS::GFP]	This study	PS10449 (*srd-1* reporter; *pkd-2* driver; GFP effector)
syIs912[srd-1P::Gal4(sk)::VP64]	This study	PS9477 (*srd-1* driver)
syIs914[srd-1P::Gal4(sk)::VP64]	This study	PS9478 (*srd-1* driver)
syIs912[srd-1P::Gal4(sk)::VP64]; syIs300[UAS::GFP]	This study	PS9473 (*srd-1* driver; GFP effector)
syIs913[pkd-2P::Gal4(sk)::VP64]; syIs300 [15xUAS::GFP]	This study	PS9681 (*pkd-2* driver; GFP effector)
syIs838[lin-48dP::NLS::cGAL (DBD)::gp41-1::N-intein::let-858 3'UTR, srd-1P::NLS::gp41-1::C-intein::cGAL(AD)::let-858 3'UTR]	This study	PS10007 (PHD driver)

syIs838[lin-48dP::NLS::cGAL (DBD)::gp41-1::N-intein::let-858 3'UTR, srd-1P::NLS::gp41-1::C-intein::cGAL(AD)::let-858 3'UTR]; syIs300[15xUAS::GFP]	This study	PS9573 (PHD driver; GFP effector)
syIs888 [gpa-14P::NLS::cGAL (DBD)::gp41-1::N-intein::let-858 3'UTR, rig-3P::NLS::gp41-1::C-intein::cGAL(AD)::let-858 3'UTR]	This study	PS10179 (AVA driver)
syIs888[gpa-14P::NLS::cGAL (DBD)::gp41-1::N-intein::let-858 3'UTR, rig-3P::NLS::gp41-1::C-intein::cGAL(AD)::let-858 3'UTR]]; syIs300[15xUAS::GFP]	This study	PS10087 (AVA driver; GFP effector)
syIs564 [odr-10P::Gal4(sk)::VP64]; syIs300 [15xUAS::GFP]	This study	PS8293 (AWA driver; GFP effector)
syIs340 [15xUAS::hChR (H134R)::EYFP::let-858 3'UTR]; him-5 (e1490) V	This study	PS9782 (Chrimson effector; *him-5*)
syIs340 [15xUAS::hChR (H134R)::EYFP::let-858 3'UTR]; him-5 (e1490) V	This study	PS7043 (Chrimson effector)
syIs371[15xUAS::HisCL::SL2::GFP::let-858 3'UTR]	This study	PS7199 (HisCL effector)
syIs612[15xUAS::GCaMP7b::SL2::mKate2]	This study	PS9046 (GCaMP7b effector)
syIs912[srd-1P::Gal4(sk)::VP64]; syIs612[15xUAS::GCaMP7b::SL2::mKate2]	This study	PS9680 (*srd-1* driver; GCaMP7b effector)
syIs912[srd-1P::Gal4(sk)::VP64]; syIs371[15xUAS::HisCL::SL2::GFP::let-858 3'UTR]	This study	PS10005 (*srd-1* driver; HisCl effector)
syIs912[srd-1P::Gal4(sk)::VP64]; syIs340 [15xUAS::hChR (H134R)::EYFP::let-858 3'UTR]; him-5 (e1490) V	This study	PS9990 (*srd-1* driver; Chrimson effector)
syIs838[lin-48dP::NLS::cGAL(DBD)::gp41-1::N-intein::let-858 3'UTR, srd-1P::NLS::gp41-1::C-intein::cGAL(AD)::let-858 3'UTR]; syIs371[15xUAS::HisCL::SL2::GFP::let-858 3'UTR]	This study	PS10189 (PHD driver; HisCL effector)
syIs838[lin-48dP::NLS::cGAL(DBD)::gp41-1::N-intein::let-858 3'UTR, srd-1P::NLS::gp41-1::C-intein::cGAL(AD)::let-858 3'UTR]; syIs340 [15xUAS::hChR(H134R)::EYFP::let-858 3'UTR]; him-5(e1490)V.	This study	PS10187 (PHD driver; Chrimson effector)
syIs888 [gpa-14P::NLS::cGAL (DBD)::gp41-1::N-intein::let-858 3'UTR, rig-3P::NLS::gp41-1::C-intein::cGAL(AD)::let-858 3'UTR]; syIs612[15xUAS::GCaMP7b::SL2::mKate2]	This study	PS10181 (AVA driver; GCaMP7b effector)
syIs564 [odr-10P::Gal4(sk)::VP64]; syIs340 [15xUAS::hChR (H134R)::EYFP::let-858 3'UTR]	This study	PS9387 (AWA driver; Chrimson effector)
hpIs675 [rgef-1P::GCaMP6s::3xNLS::mNeptune + lin-15(+)]; lin-15(n765) X; him-5 (e1490) V	This study	ZM9627 (pan-neuronal nucleus localized mNeptune and GCaMP6s)
hpIs675 [rgef-1P::GCaMP6s::3xNLS::mNeptune + lin-15(+)]; lin-15(n765) X; him-5 (e1490) V; srd-1(eh1)	This study	PS10450 (pan-neuronal nucleus localized mNeptune and GCaMP6s in *srd-1(eh1)* background)

lite-1(ce314); JAC66[ift-20P:BFP; eat-4P::cyOFP1; unc-17P::mScarlet: acr-5P::BFP; hpIs675 [rgef-1P::GCaMP6s::3xNLS::mNeptune + lin-15(+)]; lin-15(n765) X	This study	ADS1046 (pan-neuronal nucleus localized mNeptune, GCaMP6s, and neuron ID markers)
lite-1(ce314); JAC66[ift-20P:BFP; eat-4P::cyOFP1; unc-17P::mScarlet: acr-5P::BFP; hpIs675 [rgef-1P::GCaMP6s::3xNLS::mNeptune + lin-15(+)]; lin-15(n765) X; syIs912[srd-1P::Gal4(sk)::VP64]; syIs340 [15xUAS::hChR(H134R)::EYFP::let-858 3'UTR]; him-5(e1490).	This study	PS10153 (pan-neuronal nucleus localized mNeptune, GCaMP6s, neuron ID markers; *srd-1* driver; Chrimson effector)
Kp1368 [myo-2P::NLS::mCherry]; syIs371[15xUAS::HisCL::SL2::GFP::let-858 3'UTR]	This study	PS8720 (muscle driver; HisCl effector)
syIs334 [rabP::GAL4::gp41::N::let-858 3' UTR]; syIs340 [15xUAS::hChR(H134R)::EYFP::let-858 3'UTR]; him-5(e1490).	This study	PS8026 (pan-neural driver; Chrimson effector)
Software and algorithms		
Fiji	Schindelin et al., 2012 [112]	https://imagej.net/software/fiji/
MaMuT 0.27	Wolff et al., 2018 [113]	https://imagej.net/plugins/mamut/
Target track	Park et al., 2018 [114]	https://www.nature.com/articles/s41592-023-02096-3
Ilastik software	Berg et al., 2019 [115]	https://www.ilastik.org
Other		
cGAL-UAS bipartite expression toolkit	Nava et al., 2023 [116]	https://www.pnas.org/doi/full/10.1073/pnas.2221680120

621

622 **Worm Strains**

623 Strains of *C. elegans* used in this study originated from the N2 (Bristol) wild-type lineage and were
624 maintained under standard laboratory conditions using Nematode Growth Medium (NGM) plates with *E.*
625 *coli* OP50 as the food source. Detailed information regarding the strains is provided in Key Resource
626 Table.

627 **Microscopy and Imaging**

628 Animals were immobilized on a 4% ultrapure agarose pad using 3-5 µL of 2-5 mM levamisole. The
629 imaging was conducted using an inverted laser scanning confocal microscope, Zeiss LSM 980, integrated
630 with a Zeiss Axio Observer 7 with Definite Focus 2. Subsequent image processing was executed via FiJi
631 (ImageJ) software.

632 **Inhibition of PHD Neurons by the HisCl method and Modified Chemoattraction Assay**

633 Inhibition of PHD neurons was achieved through the histamine-gated chloride channel method, as
634 outlined in the study [117], with slight alterations. Nematode Growth Medium containing histamine (NGM-

635 HA) was prepared by incorporating histamine dihydrochloride from Sigma Aldrich (1 M stock solution)
636 into NGM agar at approximately 65 °C just prior to plate pouring. Control plates without histamine were
637 prepared simultaneously from the same batch of NGM. Plates supplemented with 10 mM histamine
638 remained effective for a minimum of two weeks when refrigerated at 4 °C, verified by preliminary testing
639 with a control strain possessing the *myo-2* promoter-driven HisCl effector in the cGAL-UAS system. L4-
640 stage males were selected and isolated a day in advance of the assays. Histamine treatments were
641 conducted without the presence of food to eliminate confounding factors. Histamine-induced inhibition
642 occurred within ten mins of exposure. Once removed from histamine, the animals typically require one
643 to two hours to fully recover.

644 The chemoattraction assay plates were prepared using 1.5% agar, 25 mM NaCl, 1.5 mM Tris-base, and
645 3.5 mM Tris-Cl, and conducted according to the protocol described in the literature [4], but included
646 modifications to accommodate different plate dimensions, adjustments in the spatial distance between
647 the stimulus source and the starting point of the animals, and alterations in the sex pheromone
648 concentration, as depicted in the associated figures (see Figure 1 and S1).

649 Stimulus droplets are placed on the lid of the plate, and the location of the worms is recorded every 5
650 mins up to 30 mins post-stimulation to assess their response to the introduced stimulus. In our research,
651 we utilized two sizes of plates for the assays, with effective worm-moving surfaces measuring 5.5cm and
652 8.4cm in diameter. For simplicity and clarity in labeling, these were referred to as 6-cm and 8-cm plates,
653 respectively. In our study, we employed two types of 2D chemoattraction assays distinguished by the
654 setup and calculation of the Chemoattraction Index (C.I.). For Type 1 assays, constrained by the smaller
655 plate size, a control buffer spot was not included. Here, the C.I. was derived from the ratio of worms that
656 reached the test spot to the total number of worms introduced. Conversely, in Type 2 assays, the C.I. was
657 determined by subtracting the number of worms that reached the control spot from those that arrived
658 at the test spot, divided by the total number of worms. In each chemoattraction assay, we placed 20
659 worms at a designated starting point. To ensure the reliability and robustness of our data, we repeated
660 each assay 20 times across three distinct days.

661 **Chemoattraction Assay**
662 Male chemotaxis was quantified using a chemoattraction assay as previously described (Wan et al.,
663 2024). Briefly, 2 µL of pheromone extract or M9 buffer (control) was applied to designated spots on the
664 assay plate, each supplemented with 1 M sodium azide to immobilize responding males. 20 one-day-old
665 adult males were placed at the origin point, and chemoattraction index (C.I.) were calculated after 30
666 minutes using the formula: $C.I. = (E - C) / (E + C + N)$, where E, C, and N represent the number of worms
667 at the experimental, control, or neither spot, respectively. PHD-inhibited worms prepared via the
668 "Inhibition of PHD Neurons by HisCl Method" .

669 3D chemoattraction assay employing 0.3g of gellan gum in 100ml chemoattraction assay buffer to create
670 a navigable gel environment. This composition ensures that worms can navigate through the gel freely,
671 without becoming immobilized by water or causing structural damage to the gel through movement. The
672 gellan gum solution is adjusted to match the salt concentration of the chemoattraction assay plates
673 utilized in this research.

674 For plate preparation, 22 ml of the gellan gum solution is poured into a 6-cm plate immediately after the
675 gellan gum is dissolved by heating in a microwave. The solution is allowed to cool to room temperature
676 before introducing the worms. To embed the worms within the gel, 0.5ml of the gellan gum gel is

677 removed from the center of the plate by pipetting. Then, 20 worms are picked by worm picker and
678 placed. This cavity is then refilled with 0.7 ml of gellan gum gel, ensuring the worms are fully embedded
679 within the gel. Unlike traditional chemoattraction assays, the stimulus is applied directly onto the surface
680 of the gel rather than on the lid of the plate (see Figure 2B). This approach ensures that the pheromone
681 remains accessible to the worms and provides a localized and consistent gradient for them to follow. In
682 this endpoint assay, trajectories are not recorded; instead, the number of worms reaching the target
683 spot is documented every 5 minutes for up to 30 minutes post-stimulation to evaluate their responses to
684 the introduced stimulus. This scoring method focuses on the culmination of navigational behavior,
685 capturing the effectiveness of the worms' ability to detect and respond to the pheromone gradient over
686 time. To ensure the reliability and robustness of our data, we repeated each assay 20 times across three
687 distinct days. PHD-inhibited worms were prepared via the "Inhibition of PHD Neurons by HisCl Method".
688 We remark that this C.I. quantification is not a projection onto the 2D plane, since worms at the target
689 will stay still afterwards but those not reaching the target will move in all directions. For example, a
690 worm at the same (x,y) coordinate as the pheromone location but vertically below the stimulus droplet
691 (so the z coordinate is different from the droplet) will continue to move around and will not be counted
692 when computing the C.I. To control for vertical bias, the control solution and pheromone are placed on
693 the same z-plane, preventing preference for movement toward the surface or bottom. Therefore, the C.I.
694 reliably identifies worms at the target location in 3D space.

695 **Optogenetics Perturbation Velocity Analysis**

696 The optogenetics perturbation assay was conducted using Chrimson, a red-shifted channelrhodopsin,
697 following protocols outlined by the literature [82,118,119], with slight modifications. All-trans-retinal (Sigma-
698 Aldrich) was incorporated at a concentration of 500 µM into 6-cm diameter plates containing 20mL of
699 chemoattraction assay solution. One-day-old adult animals were placed on these plates and subjected to
700 a red LED stimulus using a WormLab Tracking system (MBF Biosciences). Prior to stimulation, allow 5
701 worms a 5-minute acclimation period on the assay plate. The LED stimulus was administered in a pattern
702 of 5 seconds baseline record before stimulation, and 10-60 seconds on, followed by 7.5-30 seconds off,
703 at 100% intensity across 6-8 cycles. Implement a 30-second inter-stimulus interval for PHD activation.
704 This provides sufficient time for the worm to return to a stable forward movement state. Worm tracking
705 was conducted using the same WormLab system.

706 **Dissecting Micro-behaviors Under Optogenetic Perturbation**

707 Experiments used 8-cm NGM agar plates seeded with a thin OP50 layer to prevent starvation-induced
708 behaviors. Males were transferred from ATR+ and ATR-culture plates to an assay plate. The plate was
709 mounted on a motorized stage controlled by a joystick. Individual males were tracked and recorded with
710 a 10x 0.3NA Nikon Plan Fluor objective at 10Hz. Illumination was provided by dim, red-filtered light using
711 a HOYA 52 mm R(25A) filter to minimize disturbance to the worms. For the stimulation, we used a Sola
712 Light Engine (lumencor) light source and a 607/36 nm BrightLine excitation filter. The microscope's field
713 diaphragm was adjusted such that only a small area was illuminated when the excitation light was on.
714 We used the SOLA-SE2 software to control the light source. Prior to stimulation, allow a single worm for
715 a 5-minute acclimation period on the assay plate. The male was tracked manually using the motorized
716 stage and the following stimulation regime was applied: 30 seconds without light, followed by twenty 2-
717 second tail pulses (2-second intervals), another 30-second dark period, then 30 seconds of head
718 stimulation, and a final 30-second interval without light.

After postprocessing, we divided the recording into 2-second segments. For each 2-second segment, we tabulated the behavioral motif displayed by the male or the first behavioral transition that occurred during that segment. The following behavioral motifs and transitions were included: forward, backward, transition from forward to backward, transition from backward to forward movement, hesitation (marked by frequent direction changes within the 2-second window), and self-exploration (where the worm attempts to probe its own body). This analysis provides a detailed account of the nuanced responses of male *C. elegans* to optogenetic perturbation, offering insights into the micro-behavioral dynamics elicited by targeted neural stimulation.

Our analysis employs two analyses: The four-motif analysis (Figure S6) focuses on core locomotion states (forward, backward) and transitions (forward to backward, backward to forward). In the four-motif analysis, transitions (e.g., forward-to-backward, backward-to-forward) were classified based on the initial and final directions observed within the 2-second window. For example, a segment with rapid oscillations between forward and backward movement was categorized as "forward-to-backward" if the net directionality shifted from forward to backward, or vice versa.

The six-motif analysis (Figure 4) expands categorization to include self-exploratory and high-frequency direction transitions (renamed from “hesitation”), which capture other behaviors that cannot be easily classified as the “four-motif". The high-frequency direction transitions (“hesitation"), motif specifically identifies intervals with more than 2 direction changes within a 2-second window, representing a distinct exploratory strategy that cannot be unambiguously assigned to single transitions (forward to backward or backward to forward).

Sex Pheromone-Induced Pan-neuronal Calcium Imaging

For sex pheromone extraction, we processed 100 virgin *fog-2* female *C. elegans* by isolating them in 1 ml of NGM buffer within an Eppendorf tube, following a protocol slightly modified from the previous study [4]. These females were washed five times to clear bacterial contamination, then incubated in 100 µl of NGM or M9 buffer for 6 hours. A parallel extraction process utilized for *C. remanei* involved similar steps but with only 5 females.

In Figure 1C, to evaluate PHD activation upon exposure to the volatile pheromone, we performed calcium imaging with a custom-built spinning disk confocal microscope setup [49,74]. Utilizing the ZM9627 strain, which marks all neuronal nuclei with GCaMP6s and mNeptune [74] and incorporates *him-5(e1490)* mutation to enrich for males. We also crossed ZM9627 with the CB5414 *srd-1(eh1)* line. Preparation for imaging involved isolating L4 males 15-20 hours in advance, placing them on 10% agar NGM buffer slides.

The Thin Layer Micro-Diffusion (TLMD) method was adapted from Wan et al. [4] (see Figure S9A). Neuronal excitation was detected by measuring changes in fluorescence intensity using a disposable worm-mounting and a chemical-loading device called the thin-layer micro-diffusion (TLMD) unit. The TLMD unit consisted of a 4% agarose pad (0.2 mm thick, 1.3 mm radius) sandwiched between two autoclave tapes. Before mounting, well-fed transgenic worms were transferred to an empty worm plate for 5 minutes to remove residual bacteria. A 0.2 µL of 1 mM levamisole was then applied to the agarose pad to partially immobilize the worms, which were positioned uniformly with their heads facing outward. A clean 22 × 40 mm coverslip was gently placed over the TLMD unit. At the 30-second time point, 8 µL of the test chemical solution was loaded. Due to capillary action, the solution rapidly filled the space between the

slide and coverslip. Chemical diffusion began immediately (within milliseconds) as the micro-gel pad became surrounded by the loaded solution. Approximately 5 ul of 0.2 um latex beads (Polysciences, Inc.) were added to aid immobilization.

Imaging was conducted with a 40x 0.95 NA objective, achieving 200 Hz to record 10 volumes per second, with each comprising 20 optical slices. Pheromone or control buffer introduction occurred 30 seconds after initiating imaging, continuing for an additional 3.5-9.5 mins. Subsequent processing and registration allowed for tracking PHD neuron nuclei using semi-automated methods in MAMUT [112]. Intensities from GCaMP and mNeptune channels were extracted for analysis within defined ROIs, calculating neuronal activity ratios and smoothing data with Savitzky-Golay filters. The activity was quantified by normalizing GCaMP fluorescence against mNeptune. We used the ratio R=F(GCaMP)/F(mNeptune), after applying Savitzky-Golay filtering to each channel (polynomial order 1 and length 13) Relative intensity values ($\Delta R/R_o$) were calculated as $(R-R_0)/R_0$, where raw fluorescence intensity ratio (R) was extracted from the region of interest (ROI) of the target neuron in the calcium imaging data, and R_o is the baseline fluorescence, defined as the mean fluorescence during the quiescent period. Analyses were performed using custom code.

In Figure 5, our study employed the same custom-built spinning disk confocal microscope setup mentioned above and a sparse labeling markers pan-neuronal calcium imaging strain, ADS1046, which features a dual expression of the calcium indicator GCaMP6s and the red fluorescent protein mNeptune in all neuronal nuclei, alongside the *lite-1(ce314)* mutation to eliminate undesired light-induced neural activity. This strain also has sparse labeling markers (*Pift-20*:BFP, P*eat-4*:cyOFP1, P*unc-17*:mScarlet, P*acr-5*:BFP) for neuron identification. Intracellular calcium dynamics were quantified by tracking the calcium indicator GCaMP6s signals, which enhances green fluorescence intensity within cells. Concurrently, mNeptune signals were captured to serve as a reference. The intensity ratio of GCaMP to mNeptune (GFP/RFP) at each time point was plotted. To aid neuron identification, after the recording session, we acquired additional volumes using the following combination of excitation lasers and emission filters: 30% 640 nm 617/73 nm (200 Hz), 40% 561 nm 578 nm (200 Hz), 35% 488 nm 578 nm (200 Hz), 15% 488 nm (200 Hz), 95% 405 nm 440 or 450 nm (50Hz).

We fit the activity of AVA neurons by a linear combination of AWA and PHD neurons by minimizing the least-squared error (Figure 5F).

Neuron Tracking

Each neuron was automatically tracked through all 3D volumes with targettrack. We first applied a strong low pass filter to blur the whole image and thresholded it to find the general location of the head or tail. After centering each volume by the region found above, we cropped a rectangular ROI that covered the whole region for 99% of the recording. Then, we manually identified AWA, ASI, AVA, AVE, PHD neurons in each recording and annotated an average of 5 frames per recording. We used targettrack [114] to automatically segment and track each neuron in every volume. We trained the 3DCN of targettrack for 10K gradient steps with a batch size of 3. The quality of the tracking was manually verified after tracking.

The xyz coordinates were used to extract pixel intensities around neuronal nuclei. These changes were then standardized against the baseline pre-stimulation background, resulting in the relative intensity values (ΔR/R0) being displayed. Data representation is in the form of mean ± standard error of the mean (s.e.m.), processed using Graphpad Prism 6 and Microsoft Excel for comprehensive analysis. Custom Matlab code was utilized for graphing, with the $\Delta R/R_0$ average depicted by a black line and the s.e.m. by

802 a gray-shaded envelope. The duration of stimulation is visually encoded on the plots with a pink color
803 bar.

804 **Pan-neuronal calcium imaging with optogenetic activation**

805 This experiment used the same sparse labeling makers, pan-neuronal calcium imaging strain mentioned
806 previously. For the experiments, males were prepared on 10% agar NGM buffer slides. Using a spinning
807 disc confocal setup, we navigated the challenge of simultaneous neuronal imaging and optogenetic
808 stimulation of Chrimson, which responds to both 488 nm and 578 nm light, by implementing a strategy
809 to exploit the GCaMP signal delay post-stimulation, as outlined in Lu et al. (2022) [120]. This involved
810 interlacing five 10-second imaging/stimulation intervals with 50-second breaks, applying 12% and 35%
811 intensities for the 488 nm and 561 nm lasers, respectively, while acknowledging potential mechanical
812 stimulation from objective movement as a confounding variable. During each 5-second
813 imaging/activation period the piezo-controlled objective was moving, whereas it was not moving
814 between these periods. We therefore cannot rule out mechanical stimulation that coincided with the
815 light stimulation as a confounding factor. To aid neuron identification, after the recording session, we
816 acquired additional volumes using the following combination of excitation lasers and emission filters:
817 30% 640 nm 617/73 nm (200 Hz), 40% 561 nm 578 nm (200 Hz), 35% 488 nm 578 nm (200 Hz), 15% 488
818 nm (200 Hz), 95% 405 nm 440 or 450 nm (50Hz).

819 The same pre-processing and neuron activity tracking via Targettrack was performed as outlined in
820 "Neuron Tracking". For each neuron, we created 3 ground truth points, 100 volumes apart. Activities of
821 PHD neurons in ATR+ and ATR- males were extracted and averaged. We calculated the correlation
822 between the mean PHD activity in ATR+ males and activity traces of other neurons in both ATR+ and ATR-
823 males. A subset of 12 neurons was identified across all males and we used Generalized Procrustes
824 analysis [121] and thin plate splines [122] to register all male tail neurons to a common coordinate space.
825 These landmark neurons were: PHDR, PHDL, PLMR, PCAR, PCAL, HOA, PVY, PDC, PVX, VD12, VA10, and
826 VA11. A visual inspection identified two regions that contain neurons highly correlated with PHD
827 (correlation cutoff >0.55). Here we refer to these regions as ROI1 and ROI2 (see Figure 5 and S6). AWA,
828 ASI, AVA and AVE are identified based on sparse labeling makers, positioning and cell body size. The
829 relative intensity values (ΔR/R0) are plotted following the methodology outlined in "Sex Pheromone-
830 Induced Pan-neuronal Calcium Imaging in *C. elegans*" with minor modifications. We normalized the
831 ΔR/R0 values for each neuron in the ATR+ and ATR- groups to a range of 0 to 1. The dashed line indicated
832 the starting point of each light stimulation.

833 **Microfluidic chip design and manufacturing**

834 The design of our microfluidic devices is accomplished using SolidWorks software, tailored to the specific
835 requirements of our experiments. The fabrication process utilizes both photolithography and
836 polydimethylsiloxane (PDMS) soft lithography, as detailed in the literature [51,123]. Initially, 3-inch silicon
837 wafers were prepared by coating with a layer of SU-8 photoresist. This layer was subsequently patterned
838 through photolithography, transforming the wafer into a mold for PDMS casting. For constructs intended
839 for male worm imaging, the SU-8 2015 photoresist was spun at 1450 rpm to achieve a thickness of 24-25
840 µm. Following PDMS casting, the microfluidic devices were bonded to glass coverslips using a plasma
841 cleaner, employing settings of 50mW power for 30 seconds to ensure a robust bond. This fabrication
842 procedure is designed to produce precise microfluidic devices, enabling the simultaneous and individual
843 delivery of stimulus to the head and tail regions of *C. elegans* males, while also facilitating concurrent
844 calcium imaging. This chip allows for accurate delivery of stimulus to both the head and tail regions

845 separately, with 4 inlets dedicated to each region and an additional outlet for waste. An optimized worm
846 trapper adaptor from a previous study [124], secures males for imaging while ensuring both ends remain
847 exposed to the stimulus channels. Designed stoppers within the tail inlet channels prevent the worms
848 from escaping during injection, without disrupting fluid flow. This approach allows for the detailed study
849 of neural responses to localized stimuli in a controlled environment.

850 **Sex pheromone preparation for microfluidics chip-based experiments**

851 To obtain large quantities of crude sex pheromone for microfluidics chip-based experiments, we
852 modified the standard extraction protocol to avoid the time-consuming isolation of L4 stage *fog-2*
853 females. We used 5-day-old *daf-22* mutant *C. elegans* hermaphrodites, which lack ascaroside synthesis,
854 to ensure the absence of confounding neuronal responses from this water-soluble sex pheromone
855 stimulus. Bleach-synchronized *daf-22* mutant worms were washed five times with M9 buffer. L1 stage
856 arrest was induced by rotating worms in M9 buffer for 12 hours before seeding on culture plates (8-cm
857 NGM with OP50, approximately 500 L1 worms/plate). Adult worms were collected after three days (at
858 the onset of egg-laying). Adults were washed from culture plates with M9 buffer and separated from
859 eggs using the precipitation method (repeated 5-7 times until eggs were absent). Separated adults were
860 transferred to new OP50-seeded plates, and this washing process was repeated for 6 days to exhaust
861 self-sperm. Sex pheromone extraction was performed as described in "sex pheromone-induced pan-
862 neuronal calcium imaging" with the following modification: instead of 100 worms/mL, we used 50 µl of
863 packed worm volume per 1 mL of M9 buffer (see Figure S10 A-C). Three batches of extracted pheromone
864 were tested for quality using a chemoattraction assay and combined to create a 100 ml homogenous
865 stimulus for microfluidics chip-based experiments.

866 **Microfluidics chip-based experiment calcium imaging and data analysis**
867 Young adult *C. elegans* males (PS10181) were loaded into a custom microfluidic chip that allows selective
868 exposure of head and tail to odor solutions of choice. Solution administration was directed by an array of
869 8 memory-shape alloy valves (Takasago Fluidics Inc., Japan) individually addressed by an ESP32
870 microcontroller. Imaging was performed using a Leica DM6000 B microscope equipped with a X-Cite
871 XLED1 Multi-Triggering LED illumination system (Excelitas Technologies) and iXon EMCCD detectors
872 (Oxford Instruments Andor). Image acquisition and microfluidic stimulation administration were
873 controlled and synchronized by a custom Python graphic interface using the Pycro-Manager interface for
874 the Micro-Manager microscope control software [125]. Time-lapse image segmentation was performed
875 using the pixel classification function of the Ilastik software and intensity values of GCaMP and RFP were
876 extracted using a custom Jupyter notebook. The calcium imaging traces were calculated as the ratio of
877 GCaMP6s/RFP fluorescence to correct for out-of-plane imaging artifacts. Because of the high background
878 activity of the AVA neuron, baseline values for the calculation of the $\Delta R/R_0$ metric were estimated using
879 the peakutils Python package. The relative intensity values ($\Delta R/R_0$) are plotted following the
880 methodology outlined in "Sex Pheromone-Induced Pan-neuronal calcium imaging in *C. elegans*," with
881 minor modifications. To quantify the effect of suppression/excitation on AVA neuron, we performed
882 area-under-curve (AUC) analysis. We first compute the baseline AVA activity by averaging over the 3 mins
883 before stimulation given at the most dilute concentration and subtract this baseline value from all
884 signals. Then we integrate the area under curve for each worm data for 2 mins after the stimulation. For
885 suppression, we only account for time intervals when the signal is lower than the baseline value; for
886 excitation, we only account for time intervals when the signal is higher than the baseline value so that to
887 naturally terminate the integration of area when the signal disappears. In Figure 6D, we compute the

linear combination of AVA neuron activities with only head or tail stimulation (AVA_{head}+AVA_{tail}) and compare that with the AVA neuron activity with simultaneous head and tail stimulation (AVA_{dual}).

Concentration field simulation

The concentration evolution inside the petri dishes was simulated using the Finite Element method. The simulated plates consist of a top layer of 4mm thick air and a bottom layer of 9mm thick agar. The diffusion coefficient of the sex pheromone was estimated $1.6\ mm^2/s$ in the air and $10^{-3}\ mm^2/s$ in the agar. The initial condition was set as concentration at the surface of the droplet $c_0 = 0.01\ mol/m^3$ while $c_0 = 0$ elsewhere. No-flux boundary condition was applied to the walls of the plate. For the dynamical simulations of worm searching, we take the 2D cross-section of the concentration field at z=-0.5 mm inside the agar (the air-agar interface is at z=0).

Navigation simulation

The navigation processes were simulated using an in-house extension of the HOOMD-Blue package. Mathematically, worm locomotion dynamics are described by the following equations:

$$d\boldsymbol{r} = \boldsymbol{Uqdt}, \boldsymbol{q} = (\cos\boldsymbol{\theta}, \sin\boldsymbol{\theta}), \boldsymbol{d\theta} = \sqrt{\boldsymbol{2D_R}}\boldsymbol{dW_S} + \boldsymbol{\gamma dW_T}.$$

Here, $\boldsymbol{r}$ is the position of the worm, U the velocity magnitude, **q** the orientation direction, D_R the rotary diffusivity of the orientation angle θ. dW_S and dW_T denote the standard Brownian motion on a circle $-\pi < \theta < \pi$ and a Poisson jump process respectively. $\boldsymbol{\gamma}$ is the intensity of the jump process, i.e., the tumbling rate. It has been observed [126] that during tumbles (large angle turns), the turning angle distribution displays a peak near π. Empirically, we represent the turning angle distribution as a mixture of uniform distribution and a wrapped Gaussian distribution:

$$T(\theta, \theta') = \alpha T_0 + (1-\alpha)T_1.$$

Here the turning kernel $T(\theta, \theta')$ is the probability of turning from θ' direction to θ direction. $T_0 = 1/(2\pi)$ is the uniform distribution and $T_1 = e^{-\frac{(\theta-\pi)^2}{2\sigma^2}}$ is a wrapped Gaussian distribution.

We adopt the following functional forms to reflect the above observed sensory neuron dynamics:

$$f_H = \frac{\dot{C}}{\dot{C}_0}\frac{1+tanh(log(C/C_0))}{2},$$

$$f_T =.$$

In the simulations, we fix $D_R = 0.02$, $\eta = 1$, $k_1 = 1/60, k_2^{H,T} = 1$.

Figures and Figure Legends

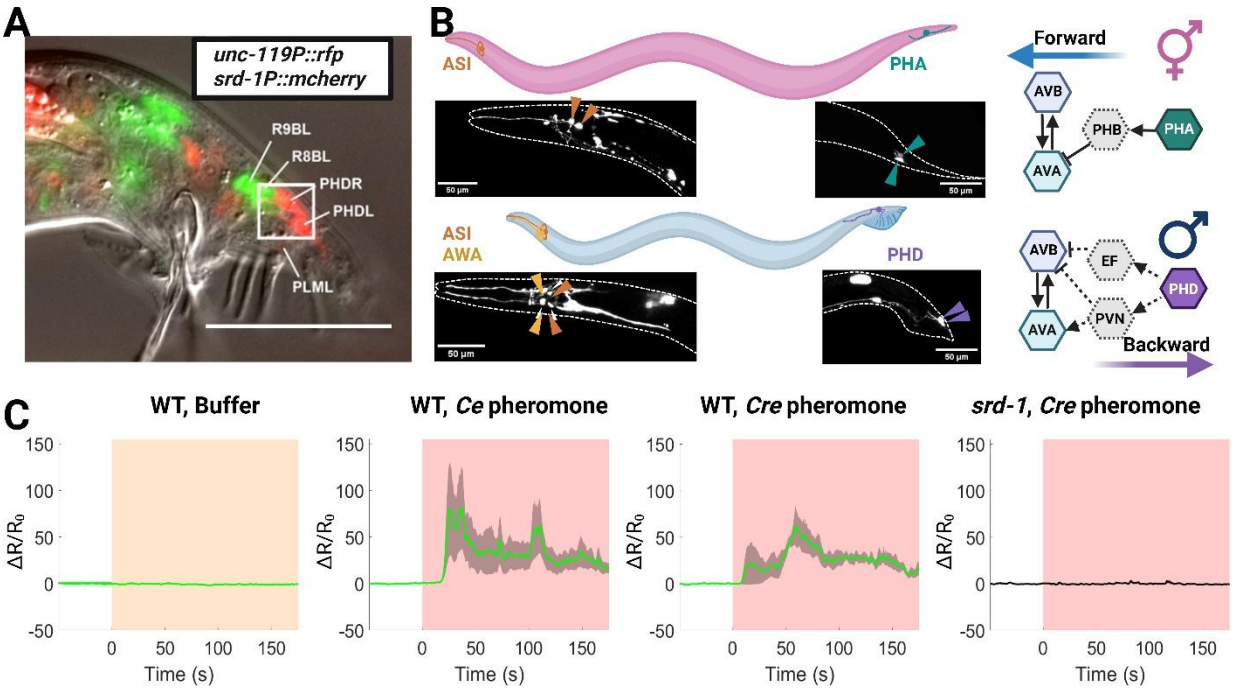

Figure 1: *srd-1* sexual dimorphism in expression patterns and male PHD neuron excitation triggered by sex pheromone depends on the chemoreceptor SRD-1. (A) Expression pattern of *srd-1*::mCherry in male tail. *srd-1* is expressed in a pair of PHD cells located in tail region of male *C. elegans*. PHD neurons are defined based on their location in the tail ganglia, and its process morphology, with P*unc-119*::rfp indicating all neuronal cell bodies. SRD-1 is not expressed in Ray B neurons (Figure S1) as reported in the literature before the existence of PHD was known[70,71]. **(B)** Sexual dimorphic expression of *srd-1* in both head and tail: *srd-1* GFP reporter expression in AWAs, ASIs and male-specific neuron PHDs in males and in ASIs and PHAs in hermaphrodites. *rab-3P::mCherry* marks all neurons; an integrated cGAL-UAS line *(srd-1P*::GAL4; UAS::GFP*)* reports *srd-1* expression. The right panel shows the expression pattern summary of *srd-1* in both males and females, along with the predicted neural circuits it might be involved in, based on their connectome and functional connectome insights. **(C)** Sex pheromone-triggered activation of PHD neurons, exhibiting SRD-1-dependent excitation, was observed through pan-neuronal calcium imaging with *rgef-1P*::GCaMP6s; a pan-neural marker (*rgef-1P*::mNeptune) indicated all neuron cell body locations (sample size: 5-7 worms per condition). Shaded areas represent the s.e.m. White indicates the pre-stimulation stage and yellow shading indicates the time window of buffer application, while pink denotes the period of pheromone application. The y-axis represents $\Delta R/R_0$, where R is defined as the fluorescence ratio of GCaMP to mNeptune.

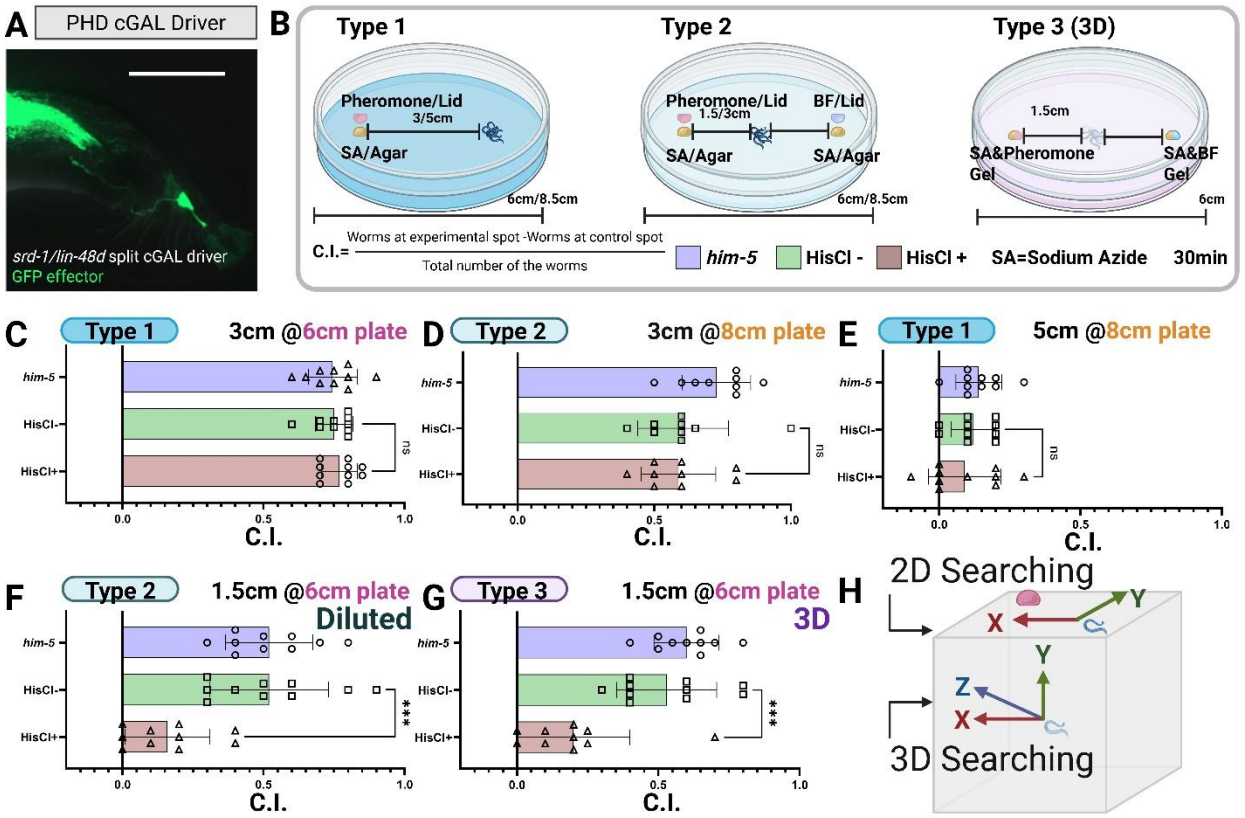

Figure 2: Exploring the role of PHD neurons in mate-searching efficiency. (A) Verification of SRD-1 expression in the PHD neuron using a split cGAL driver with *lin-48d* and *srd-1* promotor. This approach also generated a PHD-specific driver for targeted manipulation of the PHD neuron. Male tail image of cGAL-UAS line: *lin-48d*p::NLS::cGAL (DBD); *srd-1p*::NLS::cGAL (AD), 15XUAS::GFP. **(B)** Schematic representation of the chemoattraction assay and the calculation of the Chemoattraction Index (C.I.). **(C)-(G)** Impact of PHD inhibition on male mate-searching efficacy under varied task complexities. Males with HisCl induced PHDs inhibition (split cGAL-UAS bipartite system line: *lin-48dP*-NLS-cGAL (DBD); *srd-1P*-NLS-cGAL (AD) driver; UAS:: HisCl effector) can effectively locate sex pheromones in basic navigation tasks as control lines (WT and HisCl-absent sample); however, their ability to detect a 10X diluted sex pheromone and navigate through 3D environments is significantly impaired. The sample size for each assay consisted of 120 worms, 20 worms per trials, 6 trails. ***$P < 0.001$, not significant (ns): $P > 0.05$. Two-tailed unpaired t-test. Error bars represent the s.e.m. **(H)** Schematic diagram of 2D (type 1 and 2) and 3D searching (type 3).

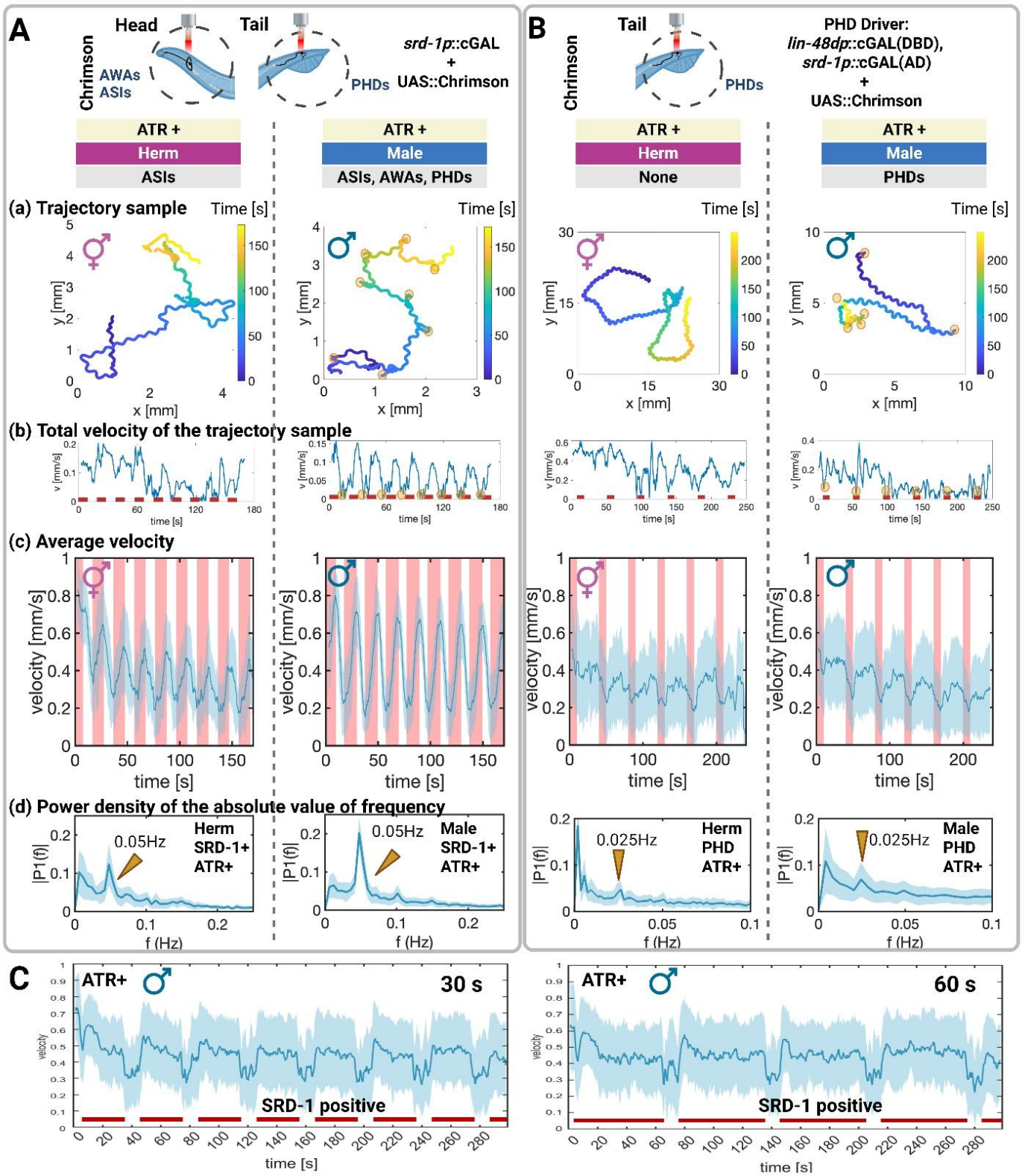

Figure 3: Contrasting locomotor responses to optogenetics activation of SRD-1 positive neurons and PHD neurons. (A)(B) Schematic diagram of the optogenetic experiment: Using *srd-1* or PHD-specific drivers

with Chrimson effector in cGAL-UAS lines, we precisely targeted the head or tail regions of freely moving males to evaluate locomotion effects. **(A)** Sex-specific locomotor responses to SRD-1 positive neuron activation in *C. elegans*. SRD-1 positive neurons (*srd-1*P-NLS-cGAL driver) were activated in both sexes using Chrimson (UAS::Chrimson effector). The stimulation protocol consisted of 12.5-second light-on intervals followed by 7.5-second light-off intervals, forming a 20-second cycle. Light stimulation is represented by the pink bar in the figure. Sample size: 120 worms. **(B)** PHD neuron activation effects on male locomotion: triggers slowdown and reversal. Targeting PHD neurons with a split cGAL-UAS bipartite system line: *lin-48dP*-NLS-cGAL (DBD); *srd-1P*-NLS-cGAL (AD) driver). The stimulation protocol consisted of 10-second light-on intervals followed by 30-second light-off intervals, forming a 40-second cycle. Light stimulation is represented by the pink bar in the figure. The sample size for the SRD-1 positive neuron and PHD neuron activation assay included 120 worms per sex. (See ATR- control in Figure S4) **(a, b)** A representative trajectory sample and its corresponding time series of instantaneous velocity magnitude, total velocity V(t), are shown. The red line indicates periods of light stimulation. The yellow circle labeled all the turning events. **(c)** V(t) averaged over 30 samples. **(d)** Fourier analysis of V(t) from Figure 2A and B demonstrates that optogenetic activation of SRD-1 positive neurons and PHD neurons produces expected peaks at 0.05 Hz and 0.025 Hz, corresponding to the 20-second and 40-second stimulation intervals, respectively. Red shade indicates light stimulation. (c), (d) Shaded areas represent the std. **(C)** Persistent enhancement of forward movement upon activation of SRD-1 positive neurons, sustained for up to 60 seconds. The stimulation protocol involved 30- or 60-second light-on intervals followed by 10-second light-off intervals. Sample size: 100 (30s stimulation) and 110 (60s stimulation) worms.

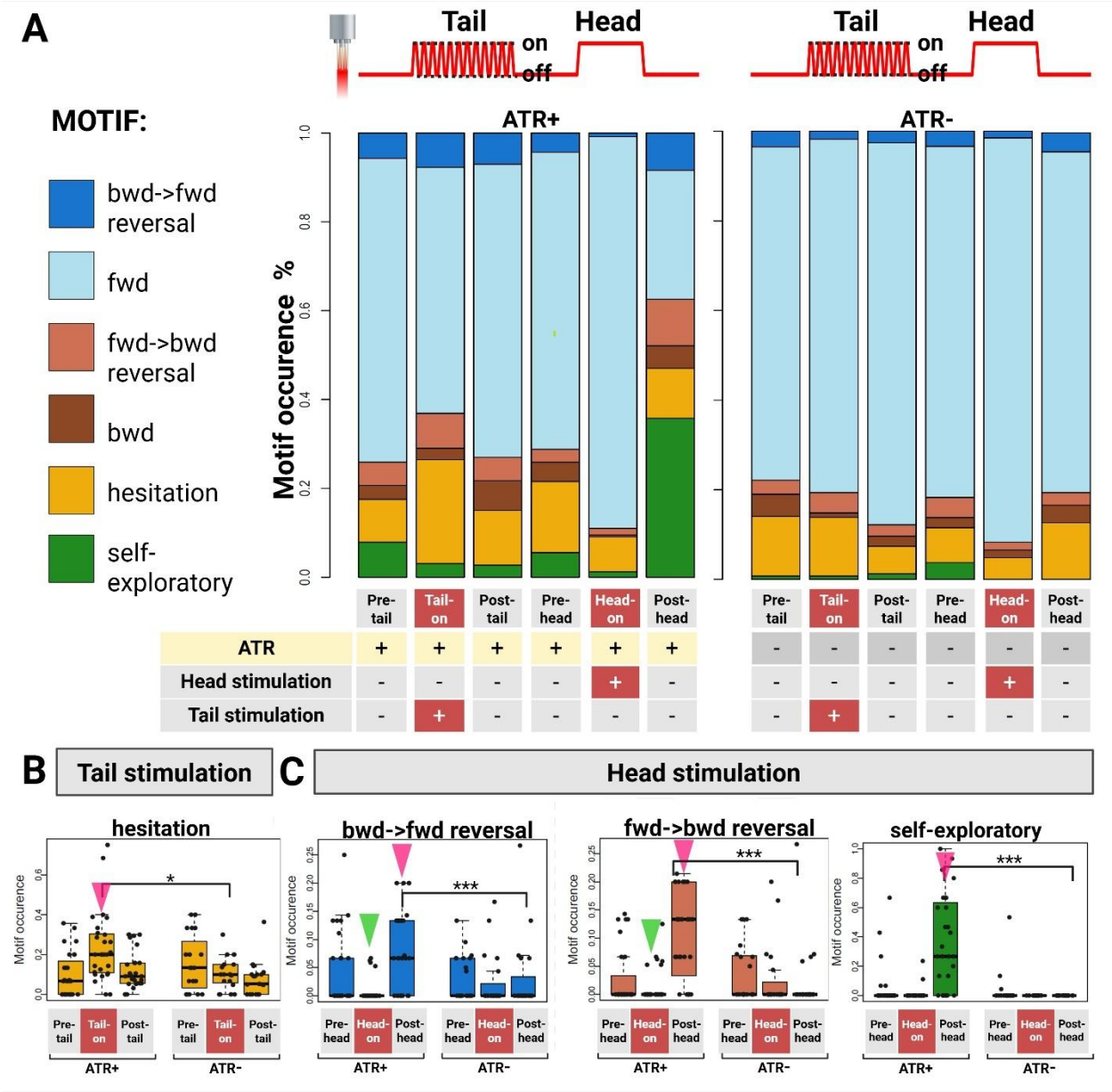

Figure 4: Six-Motif Analysis: Characterizing micro-behavioral responses to optogenetic stimulation of SRD-1 positive neurons in male *C. elegans*' anterior and posterior regions. (A) Summary of all characterized micro-behavioral and their portion among all behaviors. With *srd-1* drivers and Chrimson effectors in cGAL-UAS lines combined with region-specific light sources, we precisely targeted the head or tail regions of freely moving males to analyze locomotion effects and characterize specific micro-behaviors. **(B)-(C)** Region-specific stimulation of SRD-1 positive neurons results in varied behavioral responses, underscoring the distinct roles of these neuron groups in locomotion. **(A)-(C)** The sample size for ATR+ group consisted of 18 worms. The sample size for ATR- group consisted of 12 worms. Green arrows indicate decreases in the ATR^{+} group during stimulation relative to pre-stimulation, post-stimulation, and ATR^{-} group levels during stimulation. Pink arrows represent increases relative to the same conditions. ***$P < 0.001$; **$P < 0.005$; *$P < 0.05$.

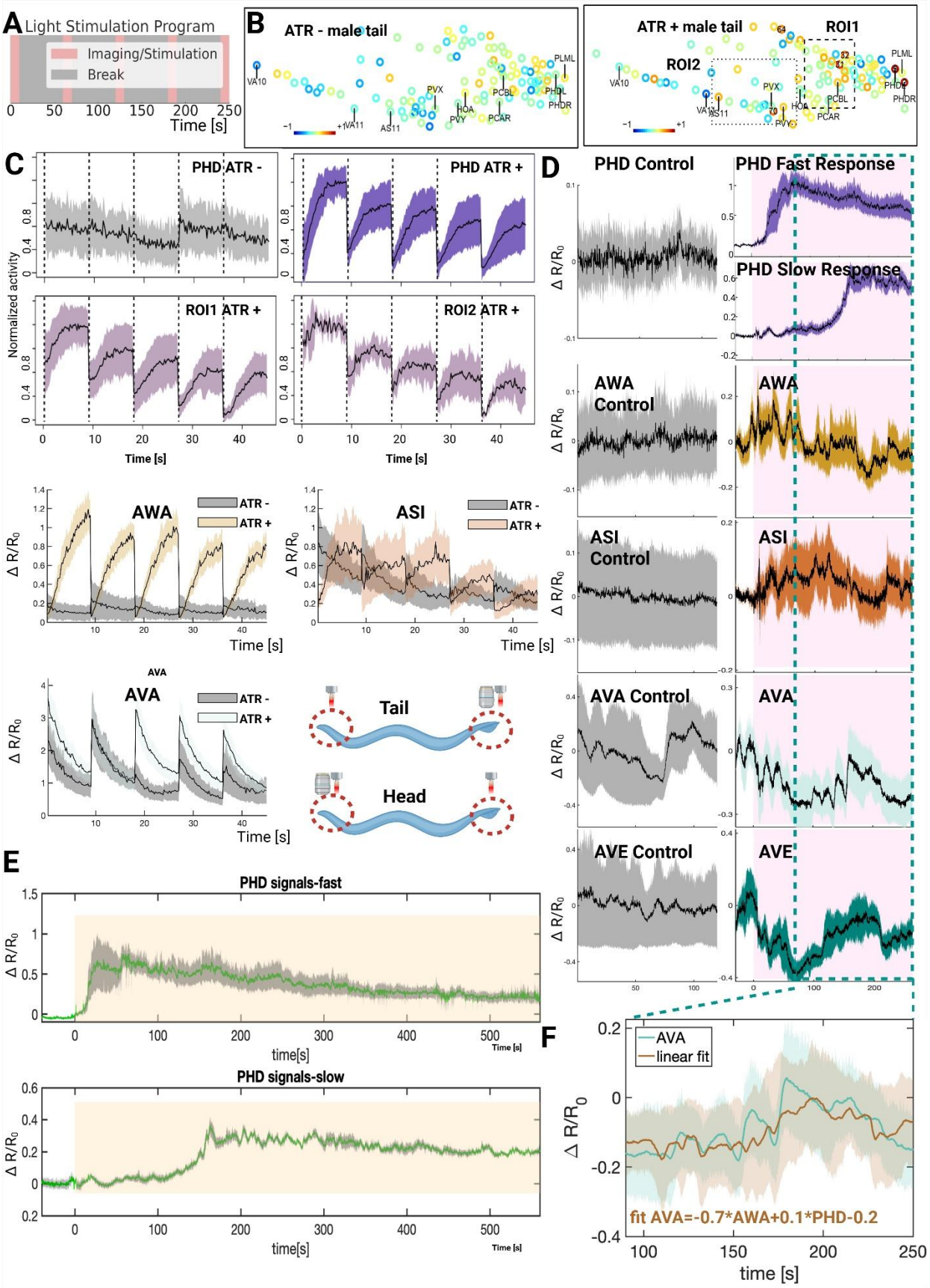
A
Light Stimulation Program
Imaging/Stimulation
Break
Time [s]
B
ATR - male tail
ATR + male tail
ROI1
ROI2
C
PHD ATR -
PHD ATR +
ROI1 ATR +
ROI2 ATR +
Normalized activity
Time [s]
AWA
ASI
AVA
ATR -
ATR +
Tail
Head
D
PHD Control
PHD Fast Response
PHD Slow Response
AWA Control
AWA
ASI Control
ASI
AVA Control
AVA
AVE Control
AVE
Δ R/R0
E
PHD signals-fast
PHD signals-slow
time[s]
F
AVA
linear fit
fit AVA=-0.7*AWA+0.1*PHD-0.2
time [s]

Figure 5: neural activation and correlation patterns following *srd-1* positive neuron optogenetic stimulation and pheromone exposure. (A) Schematic representation of the optogenetic activation protocol, consisting of five 10-second imaging/stimulation intervals interspersed with 50-second breaks. Neuronal activation of AWA, ASI and AVA neurons after optogenetic activation of SRD-1 positive neurons on head region; sample sizes: control and experimental groups (n=8 each). **(B)** Representative activation patterns were observed in male tail neurons upon optogenetic stimulation of SRD-1 positive neurons. Through visual analysis, two regions, designated as ROI1 and ROI2, were identified as containing neurons with strong correlations to PHD activity (correlation coefficient >0.55) (See Figure S6 and S7). The sample sizes: control (n=9) and experimental (n=12). **(C)** Top row: PHD neurons exhibited increased activity upon light stimulation of all SRD-1 positive neurons in the tail region in ATR+ males, but not in ATR- males. Second row: traces of neuronal activities of neurons correlated with PHD ATR+, in two regions (ROI1 and ROI2) which often contain neurons strongly correlated with PHD. The sample sizes: control (n=9) and experimental (n=12) (See Figure S6 and S7). Third and Forth row: neuronal activation in male head regions after optogenetic activation of all SRD-1 positive neurons; sample sizes: control and experimental groups (n=8 each, See Figure S9). **(D)** Calcium responses of PHD neurons over 9.5 mins of pheromone stimulation, with data grouped by response initiation time into two categories. The sample sizes are 13 worms. **(E)** Calcium responses in PHD, AWA, ASI, and reversal commanding neurons AVA and AVE upon 250 seconds of pheromone stimulation in both tail and head regions. Sample sizes for both regions are control (n=5) and experimental (n=8). (B), (C), and (E) Shaded areas represent the s.e.m. **(F)** Fitting AVA neural activity data using a linear combination of AWA and PHD neural activity, focusing on the period both AWA and PHD neurons activated. The best-fit equation for AVA activity is AVA activity=−0.7×AWA activity+0.1×PHD activity−0.2. This model indicates a weighted influence of AWA and PHD neuron activities on AVA neuronal response.

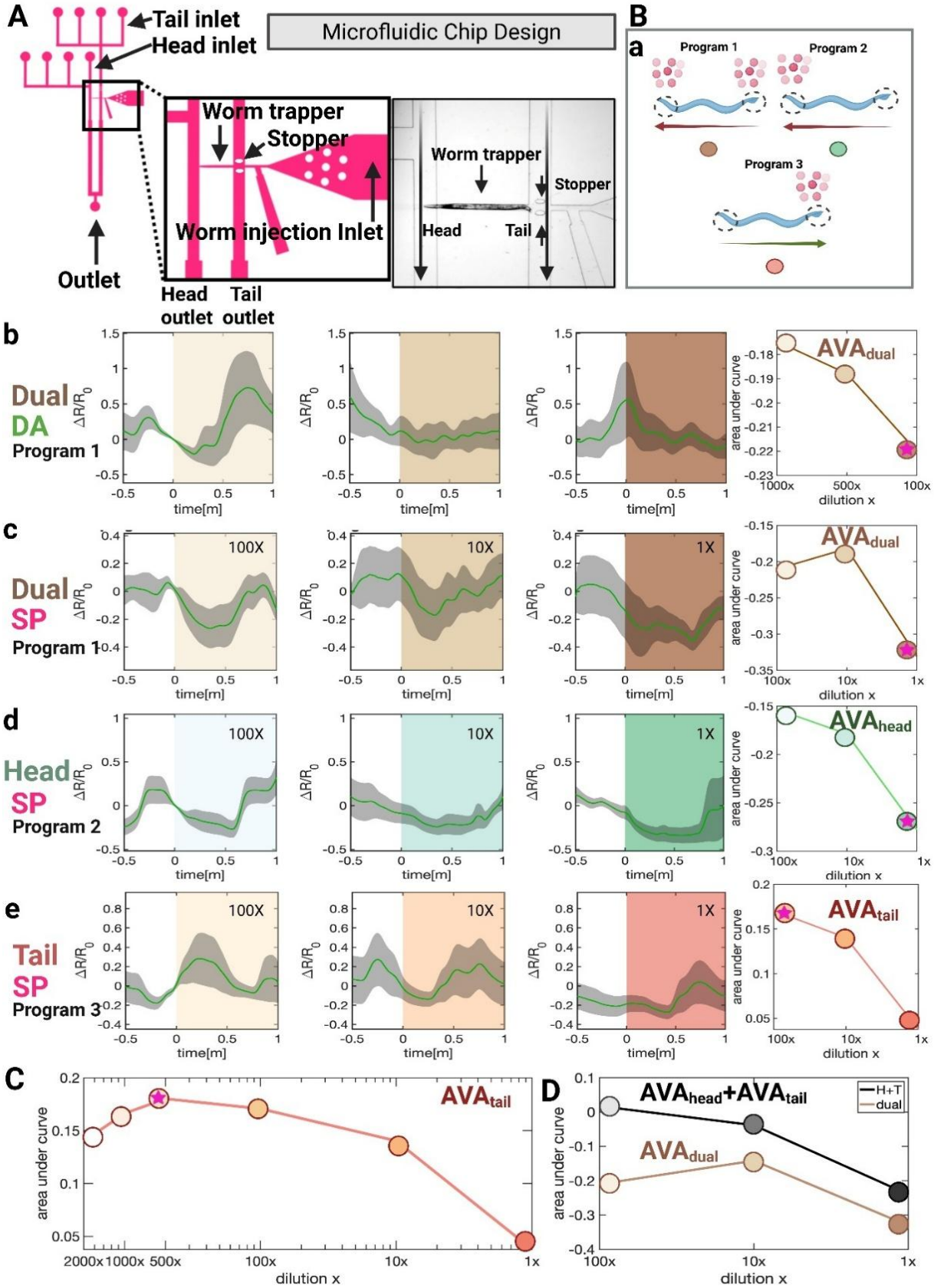

1028 **Figure 6: Dissecting reversal command neuron responses across different sex pheromone concentrations**

by microfluidics chip-based experiment (A) Schematic of the head and tail microfluidic chip designed for precise, independent delivery of target concentration stimuli to the head and tail regions separately. This chip allows for controlled, localized stimulation, enabling the delivery of different stimuli to the head and tail simultaneously. The chip includes four inlets on both the head and tail sides with a male-size-adapted worm trapper connected to a worm injection inlet. Two stoppers within the trapper intersect the tail inlet region, preventing worm escape into the tail inlet or outlet during injection. All inlets converge into a wider outlet for efficient waste and used worm collection. **(B) (a)** Schematic diagram of stimulation program and predicted behavioral outcomes. **(b)-(e)** Effects of diacetyl and sex pheromone stimulation on AVA reversal command interneuron activity in *C. elegans* males. The calcium indicator GCaMP6s was used to monitor calcium dynamics in the AVA neuron. The AVA-specific split cGAL driver construct consisted of *gpa-14P*::NLS::cGAL (DBD)::gp41-1::N-intein::*let-858* 3'UTR and *rig-3P*::NLS::gp41-1::C-intein::cGAL(AD)::*let-858* 3'UTR, paired with the GCaMP effector construct 15xUAS::GCaMP7b::SL2::mKate2. Diacetyl and dual-sided sex pheromone stimulation reduce AVA activity, as does head-specific pheromone stimulation, whereas tail-specific pheromone stimulation activates AVA neurons. Shaded areas represent the standard error of the mean (s.e.m.). The right panel shows area-under-curve (AUC) analysis (see Method), indicating that dual-sided diacetyl and sex pheromone stimulation, as well as head-specific pheromone stimulation, exert the strongest inhibitory effects on AVA at the highest tested concentration. Tail-specific pheromone stimulation produces peak AVA activation at the lowest tested concentration (100-fold dilution). **(C)** Further testing of three additional diluted concentrations reveals that tail-specific stimulation elicits the highest activation of the AVA neuron at an intermediate concentration (500-fold dilution), with activation levels decreasing at both higher and lower concentrations. Each condition (head, tail, or dual location) at each concentration was tested with a sample size of 8 worms. **(D)** The area under the curve (AUC) for AVA neuron activation resulting from head-specific stimulation combined with tail-specific stimulation closely matches the trend observed with dual stimulation alone. The hot pink star indicates the concentration that resulted in the highest inhibitory or activating effect on AVA neurons.

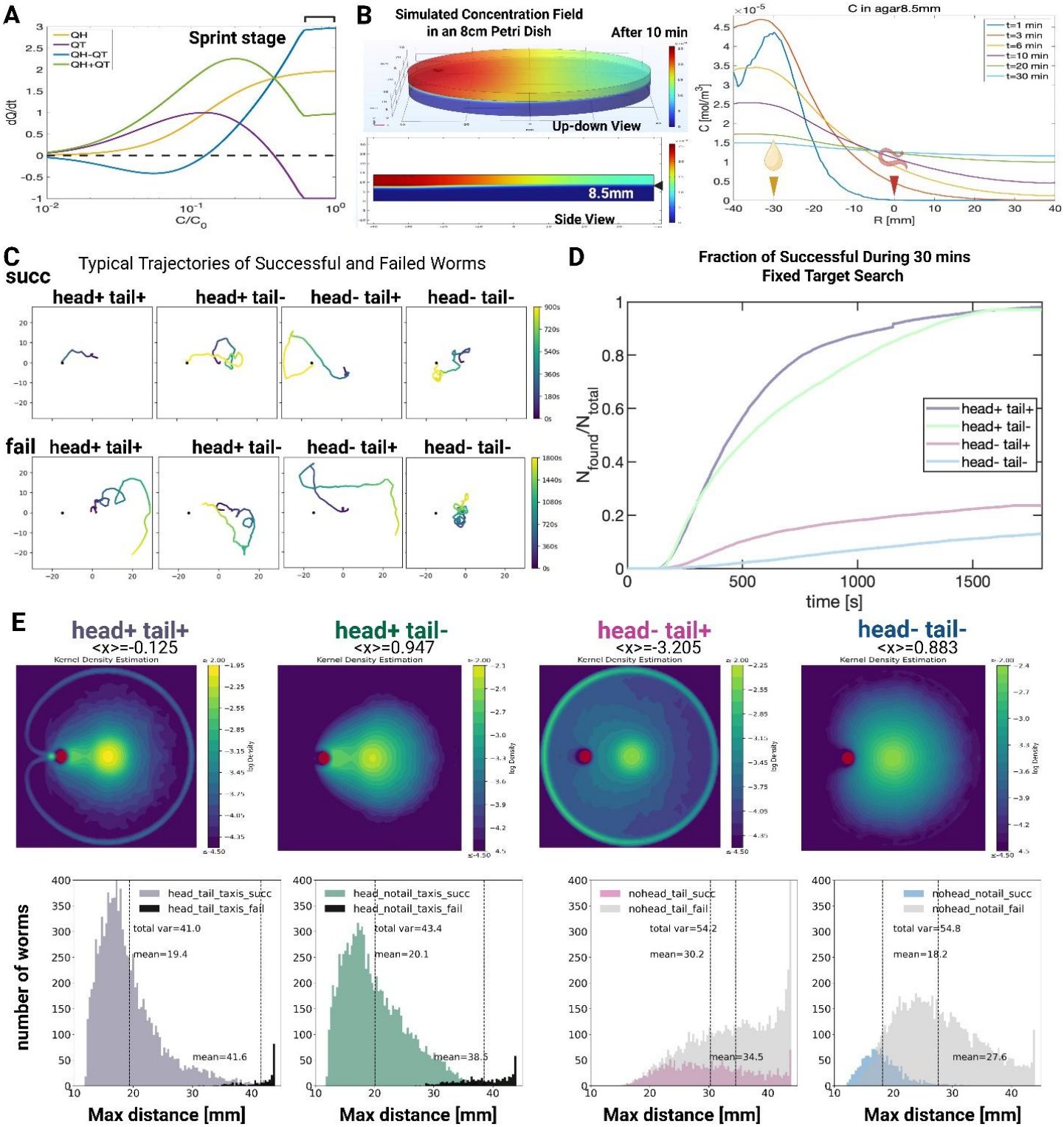

Figure 7: Simple dynamic model for a navigation mechanism with antagonistic detectors. (A) Schematic plot illustrating how confidence change rates depend on absolute concentration C in the model. C_0 is the reference concentration at the pheromone source. For head input Q^H, a fixed concentration change rate is assumed for the sensory input. At low C, both head (Q^H) and tail (Q^T) inputs accumulate slowly. At

intermediate C, tail input accumulates faster than head input. However, as C further increases, tail input starts to accumulate slower and is eventually suppressed, while head input signal is monotonically stronger as C increases until saturation at very high C. The high C regime corresponds to a large $Q^H - Q^T$ which leads to the sprint behavior. **(B)** The left panel illustrates the simulated concentration field within an 8-cm Petri dish 10 mins after stimulus introduction. The experimental setup involved placing stimulus on the lid of a Plate half-filled with agar (9mm thickness), establishing a dual-layer distribution for the volatile component. The black arrowhead marks the layer position corresponding to the details provided in the bottom panel. The right panel captures the evolution of the concentration field at the air and agar interface (8.5mm) over a 30-minute duration. **(C-E)** Simulation results to compare the roles of head and tail inputs. **(C)** Typical trajectories of successful and failed subgroups under different conditions of head/tail inhibition. **(D)** Fraction of worms that have found source during 30min search task under each condition. Tail activation results in slightly better performance for head-activated worms (compare purple and green curves) and about twice better for head-inhibited worms (compare blue and grey curves). No taxis happen under head inhibition. **(E)** The upper panel shows the simulation results comparing four head/tail input-enabled conditions, showing the spatial distributions of worms averaged over the duration of the experiments, i.e., 30 mins. The red dot shows the location of the pheromone source, and all worms start at an average distance of 15 mm to the right side of the pheromone source. The mean position along the horizontal direction is displayed as <x>. The bottom panels show the histogram of the maximum distance from the pheromone source that worms reached. The Y-axis is worm counts, and the X-axis is the maximum distance. For each of the successful and failed attempts across four different head or tail input-enabled conditions we plot the histogram from simulated data sample size of 10,000. The mean of maximum distance and total variance are indicated in each panel.

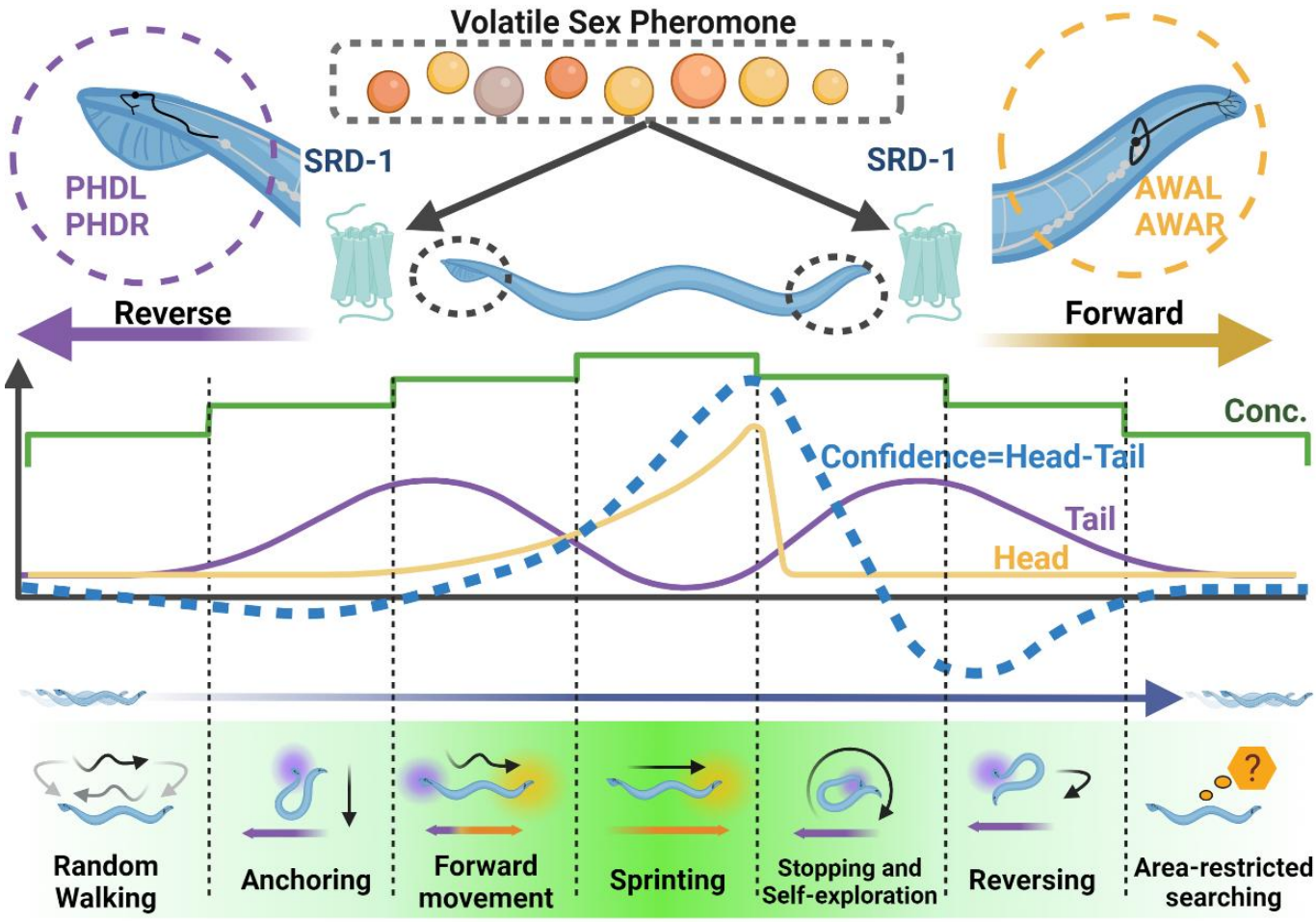

Graphical abstract:

Spatially separated pheromone detection drives adaptive navigation in *C. elegans* males.

The **upper panel** illustrates how *C. elegans* males utilize spatially separated pairs of sensory neurons, AWA (head) and PHD (tail), that detect the same volatile sex pheromone molecule via the receptor SRD-1. Despite sharing this receptor, head neurons detect gradient changes and activate when concentration increases, suppressing turning, and promoting forward movement and acceleration. In contrast, tail neurons detect absolute concentration and activate at preferred moderate concentrations, inducing reversals and deceleration. The **bottom panel** shows that upon initial pheromone introduction, simultaneous activation of head and tail neurons cancels each other out, causing males to transition from random walking to a stationary anchoring state, preventing them from chasing the concentration wave initially. As pheromone concentration increases, head neurons dominate, driving forward locomotion and acceleration. At the highest concentrations, tail neurons become less active while head neurons are highly activated, leading to rapid, goal-directed movement (sprinting). Incorrect directional choices result in AWA deactivation and persistent PHD activity, inducing pausing and local exploration. Repeated unsuccessful attempts trigger area-restricted searching.

1121 **Supplementary Figure and Legends**

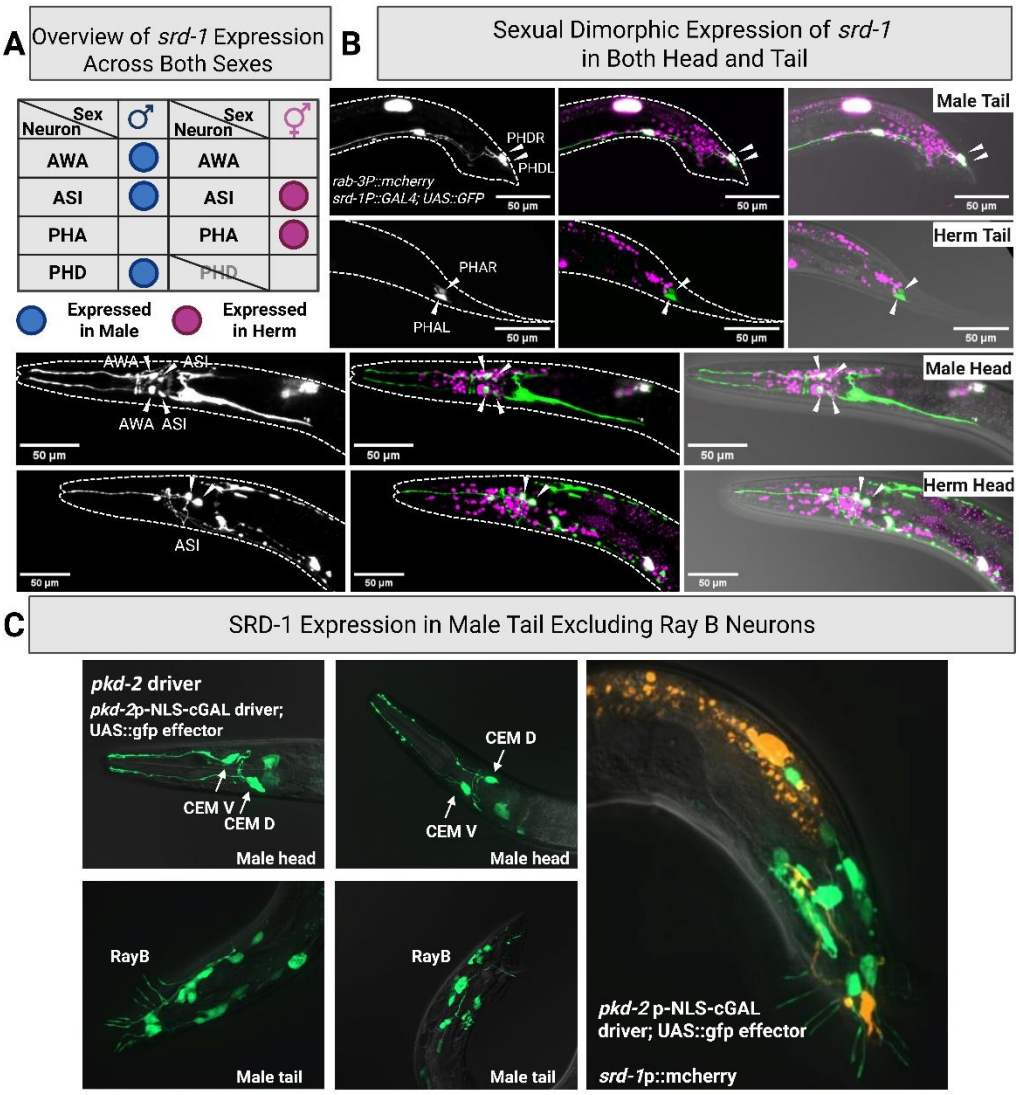

1122 **Figure S1: Localization of SRD-1 expression in the male tail, excluding ray B neurons. (A)** Overview of
1123 *srd-1* expression patterns in both sexes. **(B)** Sexual dimorphic expression of *srd-1* in both head and tail:
1124 *srd-1* GFP reporter expression in AWAs, ASIs and male-specific neuron PHDs in males and in ASIs and
1125 PHAs in hermaphrodites. *rab-3P::mCherry* marks all neurons; an integrated cGAL-UAS line *(srd-1P*::GAL4;
1126 UAS::GFP*)* reports *srd-1* expression. **(C)** Visualization of *pkd-2* expression in the male tail region using a
1127 cGAL-UAS system: *pkd-2P*-NLS-cGAL driver combined with a UAS::gfp effector. PKD-2 is known to be
1128 expressed in CEM neurons in the head and Ray B neurons in the tail. The figure presents two
1129 representative males. Absence of overlap between PKD-2 (GFP) and SRD-1 (mCherry) expressions in the
1130 male tail region, utilizing *pkd-2p*-NLS-cGAL driver and UAS::*gfp* effector in combination with *srd-*
1131 *1p*::mCherry, demonstrating distinct expression domains. **(D)** Excitation of GCaMP6s reporter in PHD
1132 neurons observed in pan-neuronal calcium imaging upon sex pheromone stimulation. PLMs are
1133 spontaneously activated before stimulation, and PHDs are activated after applying sex pheromone.

1134

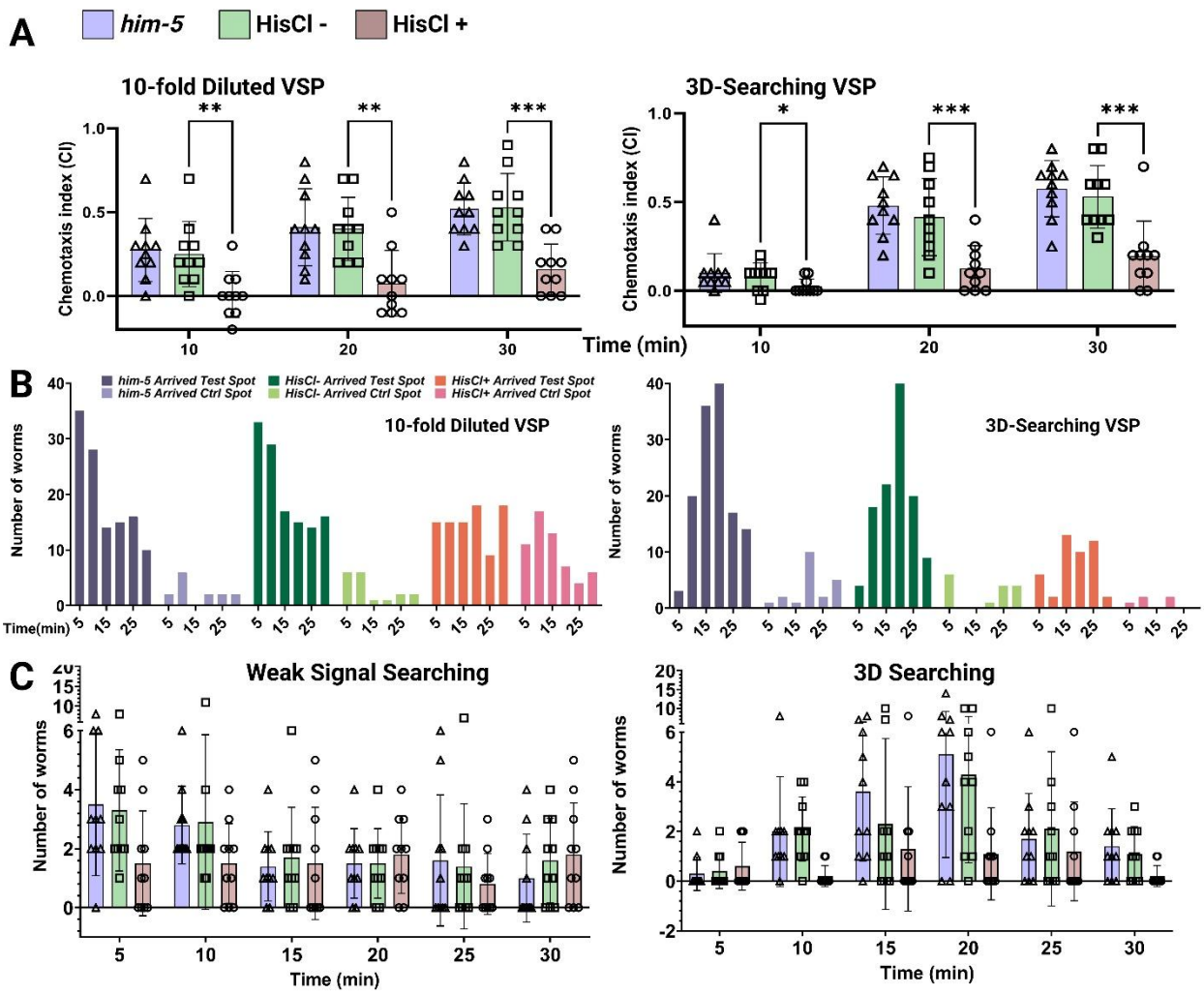

Figure S2: Chemotaxis performance of *him-5* males in weak signal and 3D searching. (A) The distribution of worms at various intervals following stimulus shows a consistently low chemotaxis index in PHD-inhibited males. **(B)** Presents the number of worms reaching a pheromone target spot at various time points during weak signal searching and 3D searching assays. The analysis of worm distribution at multiple time points after the introduction of the stimulus indicated a consistently low number of the PHD-inhibited males arrived at the test spot across all intervals, highlighting their compromised chemotactic ability. **The sample size for each assay consisted of 120 worms, 20 worms per trials, 6 trails. (C)** Different navigational deficits in PHD-inhibited males across different exploration tasks: in weak signal tasks, their even distribution between test and control spots led to a low chemotaxis index; in 3D tasks, the low index resulted from fewer males reaching the target. The sample size for each assay consisted of 120 worms, 20 worms per trials, 6 trails. *P < 0.05, **P < 0.01, ***P < 0.001, not significant (ns): P > 0.05. Two-tailed unpaired t-test. Error bars represent the s.e.m.

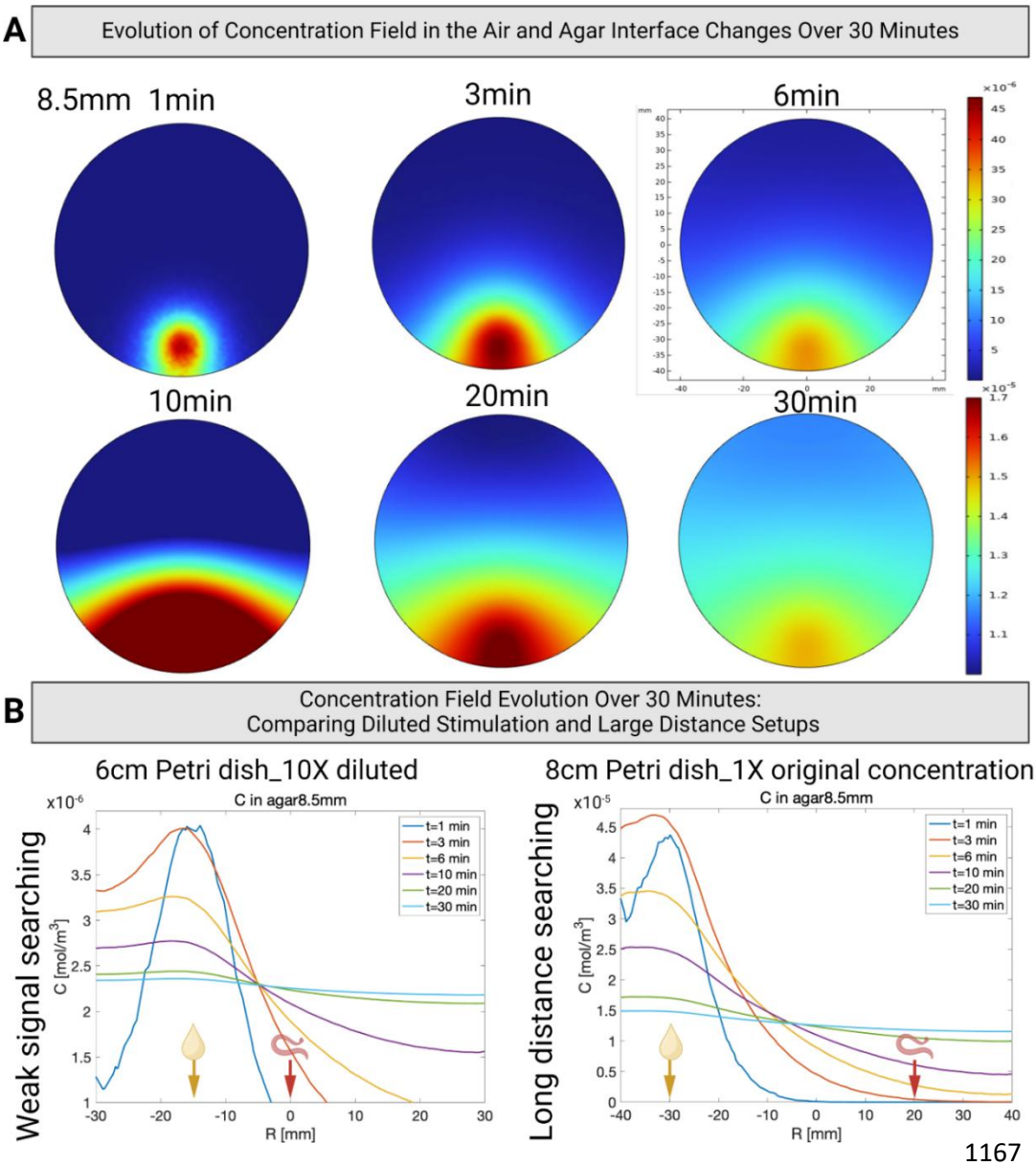

Figure S3: Visualization and dynamics of pheromone concentration fields in chemoattraction assays. (A) Captures the evolution of the concentration field at the air and agar interface (8.9mm) over a 30-minute duration. The color scales for 1min, 3min, and 6min intervals are consistent, as are those for 10min, 20min, and 30min intervals, as indicated on the right side of the panel, illustrating the dynamic changes in pheromone distribution. **(B)** Compares the evolution of the concentration field over 30 mins between diluted stimulation and large distance setups. The concentration field simulation shows that in scenarios where males are positioned far from the pheromone source, they experience areas of low absolute concentration lacking a clear gradient. In contrast, proximity to a diluted pheromone source results in a Gaussian distribution with a discernible gradient, despite the overall low concentration level, indicating different challenges in pheromone detection and navigation based on distance and concentration.

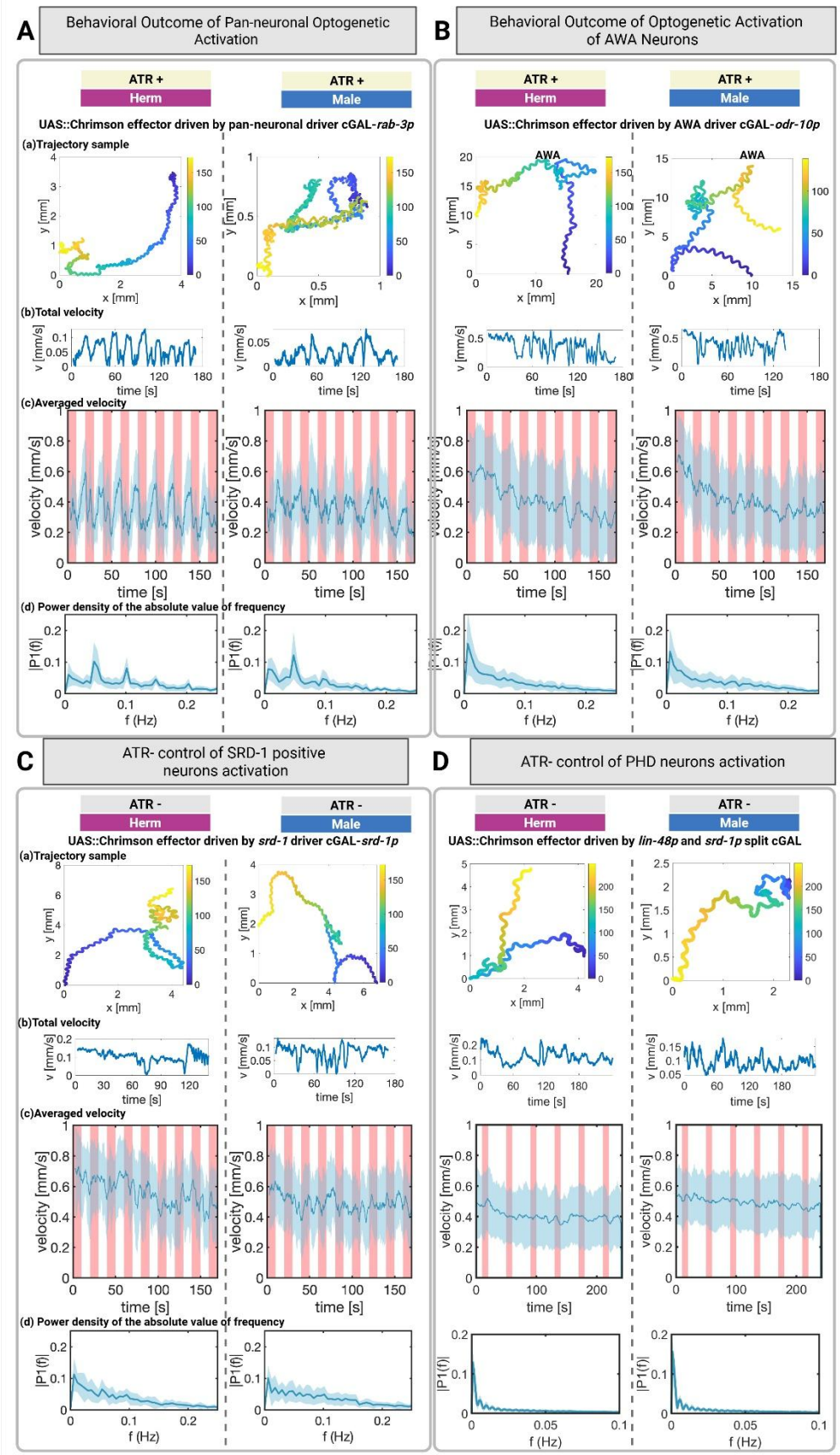
A
Behavioral Outcome of Pan-neuronal Optogenetic Activation
B
Behavioral Outcome of Optogenetic Activation of AWA Neurons
ATR +
Herm
ATR +
Male
UAS::Chrimson effector driven by pan-neuronal driver cGAL-rab-3p
UAS::Chrimson effector driven by AWA driver cGAL-odr-10p
AWA
(a)Trajectory sample
(b)Total velocity
(c)Averaged velocity
(d) Power density of the absolute value of frequency
x [mm]
y [mm]
v [mm/s]
time [s]
velocity [mm/s]
|P1(f)|
f (Hz)
C
ATR- control of SRD-1 positive neurons activation
D
ATR- control of PHD neurons activation
ATR -
Herm
ATR -
Male
UAS::Chrimson effector driven by srd-1 driver cGAL-srd-1p
UAS::Chrimson effector driven by lin-48p and srd-1p split cGAL

1179

Figure S4: Effects of Pan-Neural and AWA Neuron Activation on *C. elegans* Locomotion and ATR- Control of SRD-1 Positive Neuron and PHD Neuron Activation. (A) Demonstrates global neuronal activation via the Chrimson system in *C. elegans*, employing a pan-neuronal promoter (*rab-3p*-NLS-cGAL driver) to drive UAS::Chrimson effector expression. This approach achieved effective neuronal stimulation across the nervous system in both male and female worms, leading to a temporary cessation of movement during light exposure, with immediate resumption of normal behavior upon cessation of the stimulus. The frequency of movement cessation closely followed the stimulation protocol, showing a dominant frequency at 0.05Hz, indicating the system's effectiveness in modulating worm locomotion through pan-neural activation. **(B)** Explores the specific activation of AWA neurons and its impact on locomotion in both sexes of *C. elegans*, utilizing a targeted cGAL-UAS system (*odr-10p*-NLS-cGAL driver for AWA specificity) to activate AWA neurons. Contrary to the pan-neural activation results, selective stimulation of AWA neurons did not alter the average velocity of the worms during a 20-second period of light exposure. This outcome suggests that AWA neuron activation alone may not be sufficient to initiate forward movement, or it may reflect limitations in the activation efficacy of the *odr-10* promoter used. Notably, the frequency analysis of this experimental setup did not exhibit the expected peak at 0.05Hz. The figure includes (a)(b) a representative trajectory sample alongside its total velocity time series V(t), with the red line marking periods of light stimulation; (c) the averaged V(t) across 30 samples, highlighted by a red shade during light stimulation; and (d) the Fourier analysis of V(t), illustrating the differential response patterns to pan-neural versus AWA-specific activation. The sample size for the pan-neural activation assay included 50 worms per sex, while the AWA activation assay involved 110-120 worms per sex. Error bars represent the std. **(C)** Locomotor responses to SRD-1 positive neuron activation in both sexes of *C. elegans*. SRD-1 positive neurons (*srd-1*P-NLS-cGAL driver) were activated in both sexes using Chrimson (UAS::Chrimson effector). The control, without all-trans retinal (ATR), had no change in behavior, eliminating any light effects. **(D)** Locomotor responses to PHD neuron activation in both sexes of *C. elegans*. PHD neurons (split cGAL-UAS line: *lin-48d*P-NLS-cGAL (DBD); *srd-1*P-NLS-cGAL (AD) driver) were activated in both sexes using Chrimson (UAS::Chrimson effector). The control, without all-trans retinal (ATR), also had no change in behavior, eliminating any light effects. **(C) (D)** The sample size for the SRD-1 positive neuron and PHD neuron activation assay included 120 worms per sex (See ATR+ control in Figure 3).

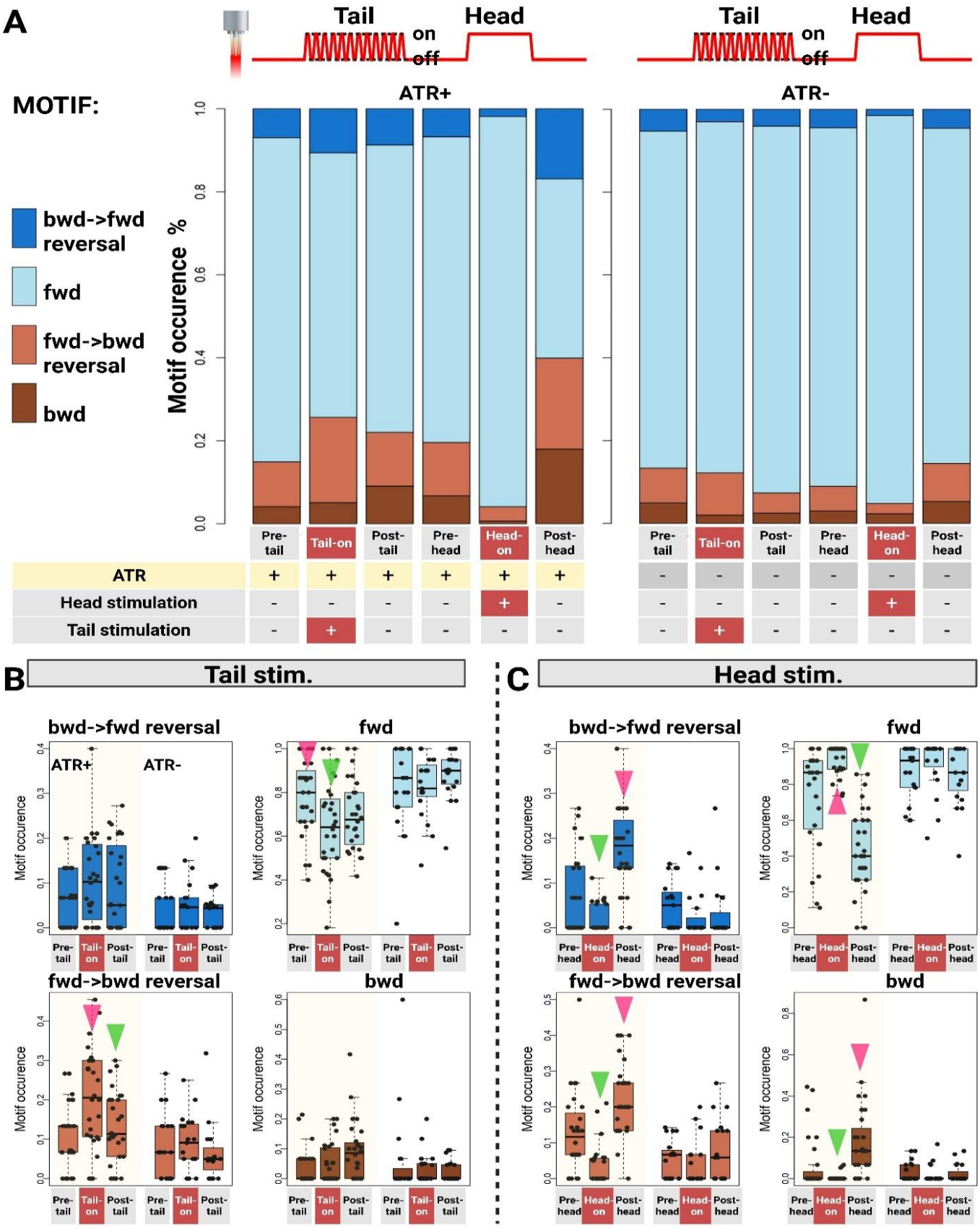
A
Tail
on
off
Head
ATR+
ATR-
MOTIF:
bwd->fwd reversal
fwd
fwd->bwd reversal
bwd
Motif occurence %
Pre-tail
Tail-on
Post-tail
Pre-head
Head-on
Post-head
ATR
Head stimulation
Tail stimulation
B
Tail stim.
C
Head stim.
bwd->fwd reversal
fwd
fwd->bwd reversal
bwd
Motif occurence

1217

1218 **Figure S5: Four-Motif Analysis: Differential locomotion responses to optogenetic stimulation of SRD-1**
1219 **positive neurons in male *C. elegans.*** Utilizes the *srd-1* Chrimson cGAL-UAS system for precise
1220 optogenetic stimulation of SRD-1 positive neurons in the head and tail regions of male *C. elegans*,
1221 revealing distinct locomotive responses. Tail-targeted light pulses induced transitions from forward to
1222 backward movement and hesitancy in movement direction. Continuous head stimulation resulted in
1223 sustained forward motion and exploratory post-stimulation behaviors. Experiments included ATR+ (n=18)
1224 and ATR- (n=12) groups, with sequential recording periods before, during, and after stimulation in both
1225 regions, to assess the nuanced impact on locomotion. **(A)** Tail activation effects on locomotion. A short
1226 light pulse targeting the tail induced a notable transition from forward to backward movement and
1227 increased hesitancy in movement direction during stimulation. **(B)** Head activation and subsequent
1228 behaviors. Continuous head stimulation for 30 seconds prompted sustained forward movement during
1229 light exposure and immediate directional adjustments post-stimulation. After head stimulation, males
1230 engaged in self-exploratory behaviors, using their tails for body probing. Each worm was recorded for 30
1231 seconds before tail stimulation, followed by a 2-second alternating light pulse targeting the tail over 12
1232 cycles. Post-tail stimulation, there was another 30-second recording period before initiating head
1233 stimulation, then the head stimulation lasted for 30 seconds. The worm was then recorded for an
1234 additional 30 seconds after the light stimulation concluded. Error bars represent the s.e.m.

1235

1236

1237

1238

1239

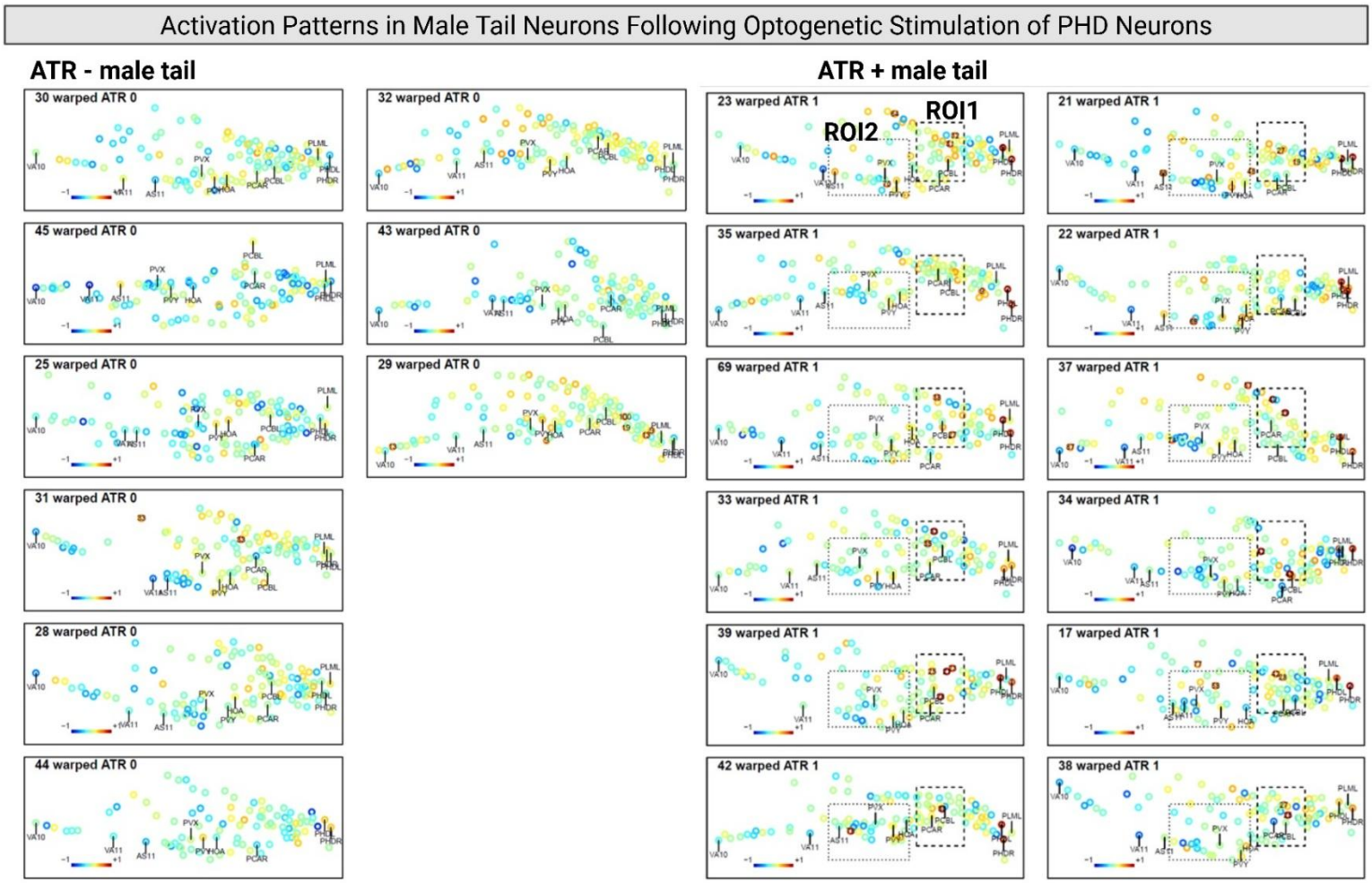

Figure S6: Activation patterns observed in male tail neurons upon optogenetic stimulation of PHD neurons. Visual analysis identified two regions, designated ROI1 and ROI2 in multiple males, which contain neurons with strong correlations to PHD activity in ATR+ group, but not ATR- group (correlation coefficient >0.55). Sample sizes: control (n=9) and experimental (n=12).

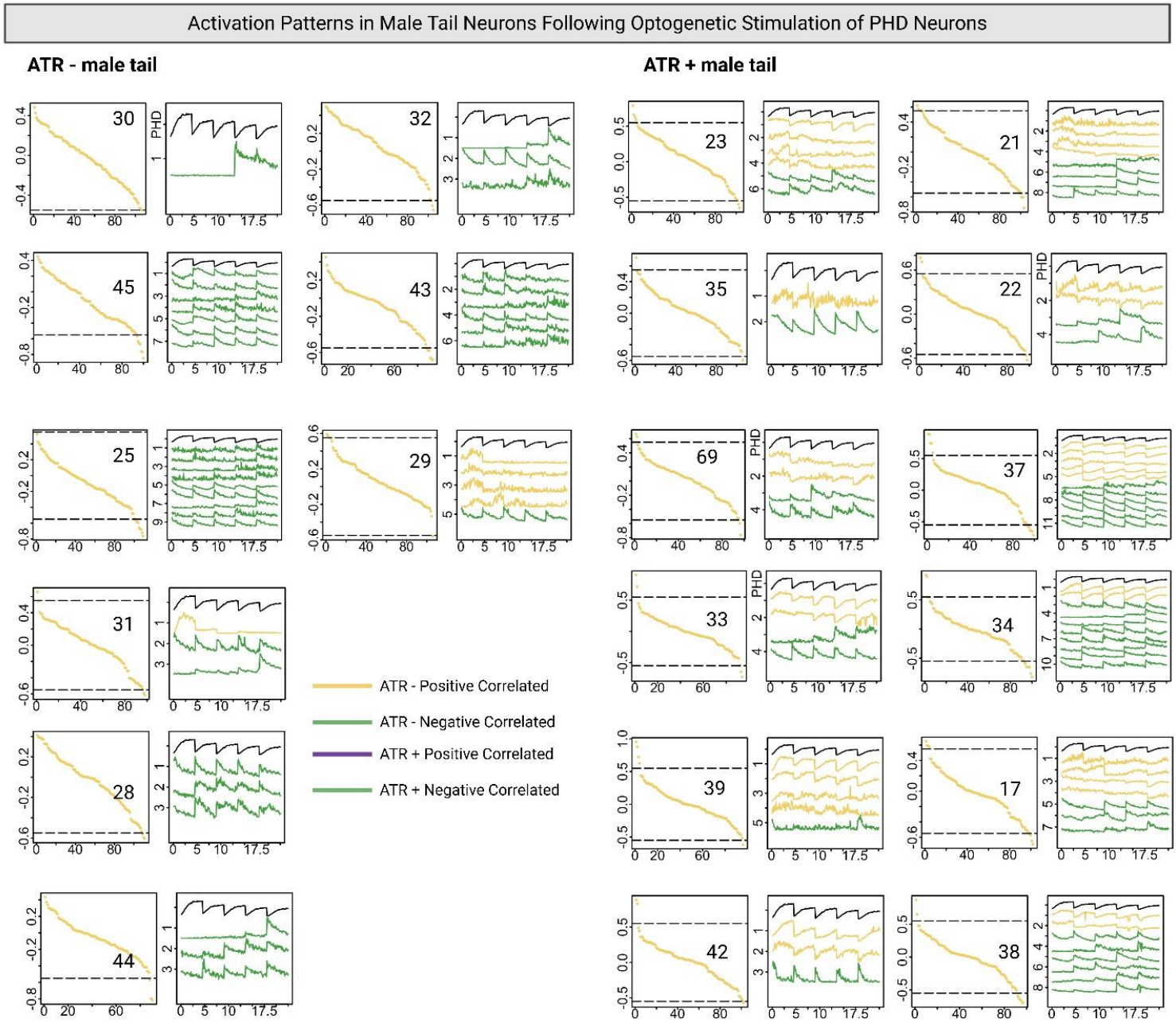

Figure S7: Neural activity correlations with PHD optogenetic stimulation in tail regions. Yellow and purple indicate positive correlations with target neuron activity in ATR- and ATR+ samples, respectively. Green denote negative correlations in ATR- and ATR+ samples, respectively. The dashed lines indicate the thresholds for positive and negative correlations. Sample sizes: control (n=9) and experimental (n=12).

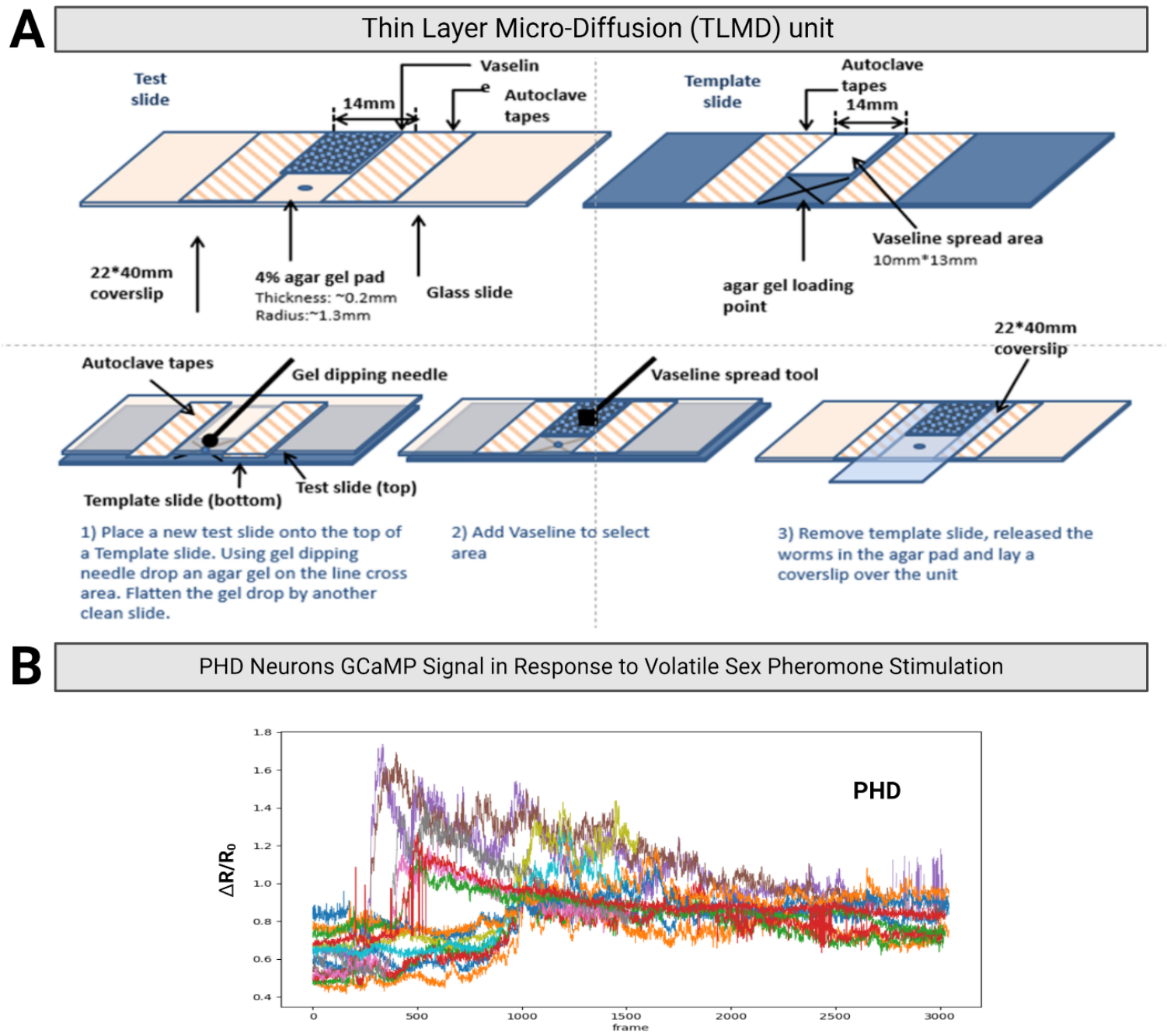

Figure S8: TLMD unit for neuronal activation and calcium response measurement. (A) Depicts the Thin Layer Micro-Diffusion (TLMD) unit setup for detecting changes in intracellular calcium signaling via GCaMP6s fluorescence intensity. The device consists of a 4% agarose pad placed between autoclave tapes, used with 0.2µl of 1mM levamisole to partially immobilize well-prepared transgenic worms. Test chemicals are introduced at 30 seconds, with rapid diffusion facilitated by capillary action. **(B)** Calcium responses of PHD neurons during 9.5 mins of pheromone stimulation, with individual animals distinguished by color coding. The sample sizes is 13 worms. Shaded areas represent the s.e.m.

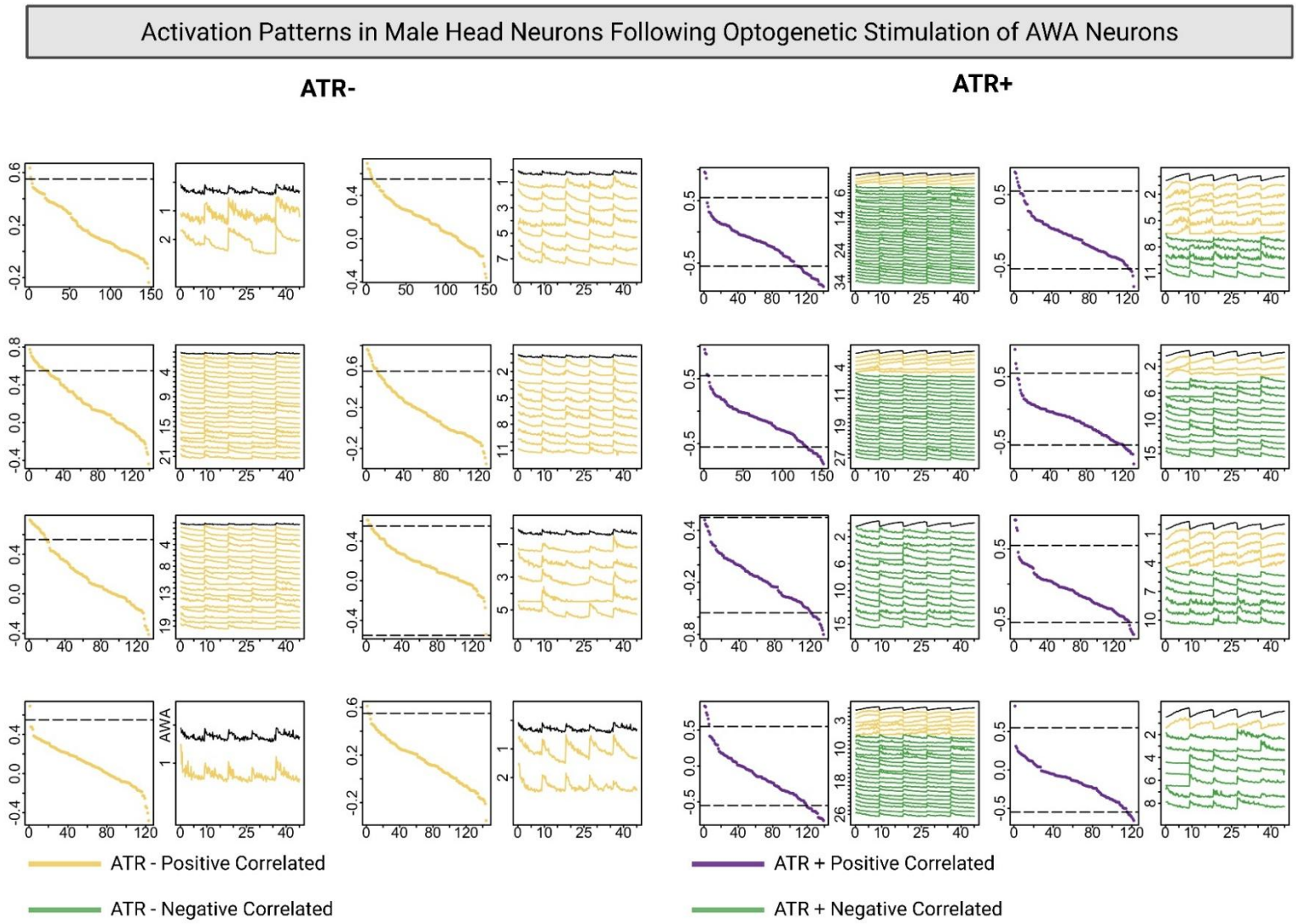

Figure S9: Neural activity correlations with AWA and ASI optogenetic stimulation in head regions. Yellow and purple indicate positive correlations with target neuron activity in ATR- and ATR+ samples, respectively. Green denotes negative correlations in ATR- and ATR+ samples, respectively. The dashed lines indicate the thresholds for positive and negative correlations. Sample sizes: control and experimental groups (n=8 each).

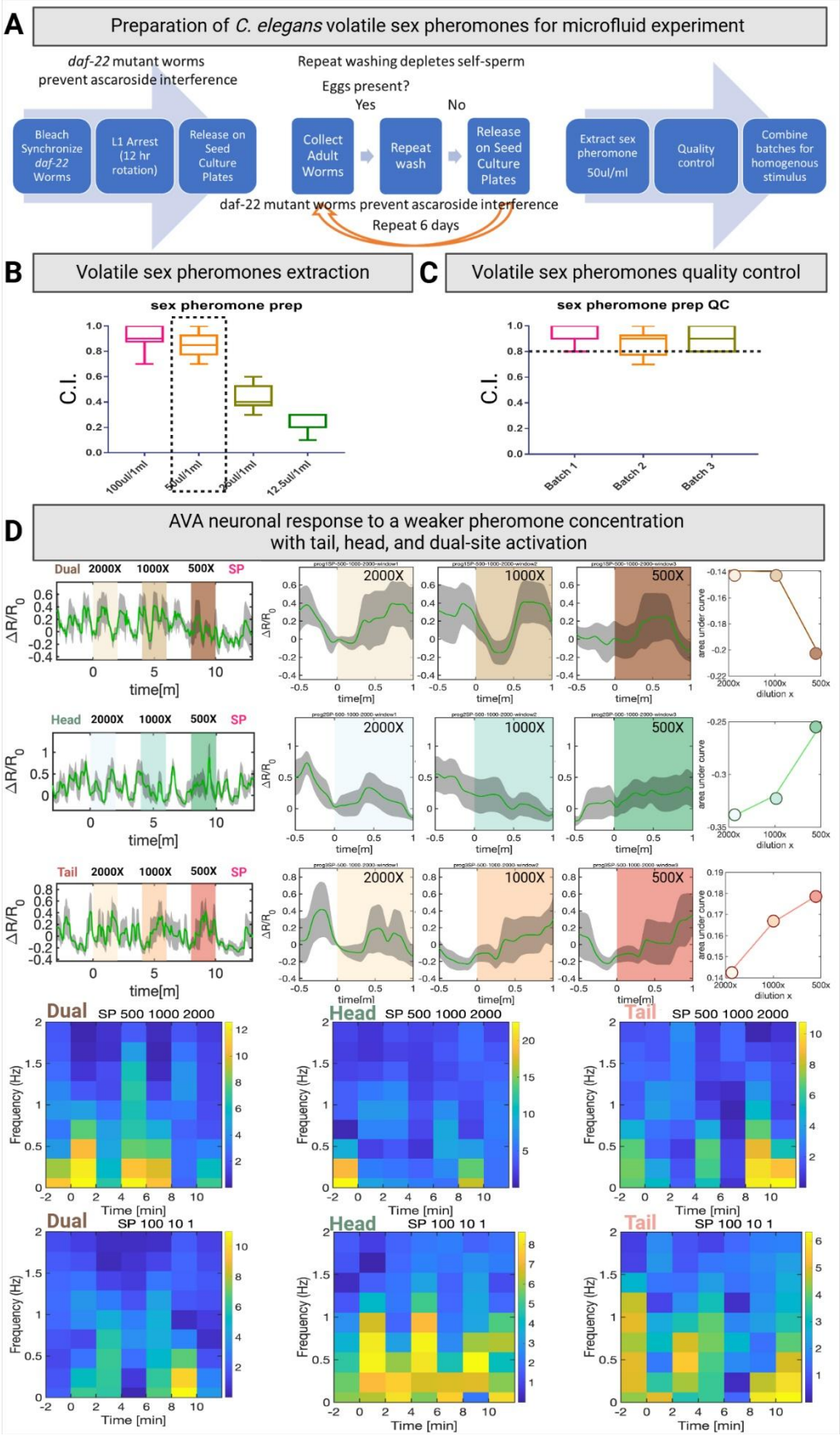
A
Preparation of C. elegans volatile sex pheromones for microfluid experiment
daf-22 mutant worms prevent ascaroside interference
Repeat washing depletes self-sperm
Eggs present?
Yes
No
Bleach Synchronize daf-22 Worms
L1 Arrest (12 hr rotation)
Release on Seed Culture Plates
Collect Adult Worms
Repeat wash
Release on Seed Culture Plates
Extract sex pheromone 50ul/ml
Quality control
Combine batches for homogenous stimulus
daf-22 mutant worms prevent ascaroside interference
Repeat 6 days
B
Volatile sex pheromones extraction
sex pheromone prep
C.I.
100ul/1ml
50ul/1ml
20ul/1ml
12.5ul/1ml
C
Volatile sex pheromones quality control
sex pheromone prep QC
Batch 1
Batch 2
Batch 3
D
AVA neuronal response to a weaker pheromone concentration with tail, head, and dual-site activation
Dual
Head
Tail
2000X
1000X
500X
SP
ΔR/R0
time[m]
area under curve
dilution x
Frequency (Hz)
Time [min]
SP 500 1000 2000
SP 100 10 1

Figure S10: Sex pheromone preparation for microfluidics chip-based experiment. (A) Modified Sex Pheromone Extraction Protocol for microfluidics chip-based experiments. To obtain large quantities of crude sex pheromone for microfluidics chip-based experiments, we streamlined the standard protocol. We used *daf-22* mutant *C. elegans* hermaphrodites, eliminating confounding ascaroside signals. Worms were synchronized and repeatedly washed to deplete self-sperm, and the sex pheromone extraction ratio was optimized. **(B)** Ratio Optimization: We tested four ratios (100µl/ml, 50µl/ml, 25µl/ml, 12.5µl/ml) for their attractiveness to males using a chemoattraction assay. The 50µl/ml ratio exhibited attractiveness comparable to 100µl/ml, with attractiveness declining at lower concentrations. Therefore, 50µl/ml was chosen for sex pheromone extraction. **(C)** Quality Control and Homogenization: Three independent batches of extracted pheromone were quality-controlled using the chemoattraction assay, all exceeding a predetermined quality threshold suggested by previous studies (C.I. = 0.8). Finally, the quality-controlled batches were combined to create a homogenous stimulus for microfluidics chip-based experiments. (B) and (C) Error bars represent the s.e.m. **(D)** Effects of sex pheromone stimulation on AVA reversal command interneuron activity in *C. elegans* males at Higher Dilutions. The calcium indicator GCaMP6s was used to monitor calcium dynamics in the AVA neuron. The AVA-specific split cGAL driver construct consisted of gpa-14P::NLS::cGAL (DBD)::gp41-1::N-intein::let-858 3'UTR and rig-3P::NLS::gp41-1::C-intein::cGAL(AD)::let-858 3'UTR, paired with the GCaMP effector construct 15xUAS::GCaMP7b::SL2::mKate2. The upper panel shows the calcium-shaded areas representing the s.e.m. This set of microfluidics chip-based experiments used 500X, 1000X, and 2000X fold diluted pheromones. The right panel shows area-under-curve (AUC) analysis (see Method). The bottom panel displays oscillation frequency distributions, revealing spontaneous oscillations in AVA neuron activity upon exposure to 500X, 1000X, and 2000X diluted pheromones. Heatmaps represent the frequency responses of AVA neurons under varying stimulation conditions. Each panel corresponds to specific activation sites (head, tail, and dual activation) and serial pheromone dilutions (set 1: 1X, 10X, 100X; set 2: 500X, 1000X, 2000X). The heatmaps depict the oscillation frequency dynamics of AVA activity over 12 mins for each stimulus program, with color coding indicating the distribution and intensity of oscillation frequencies. Each condition (head, tail, or dual location) at each concentration was tested with a sample size of 8 worms.

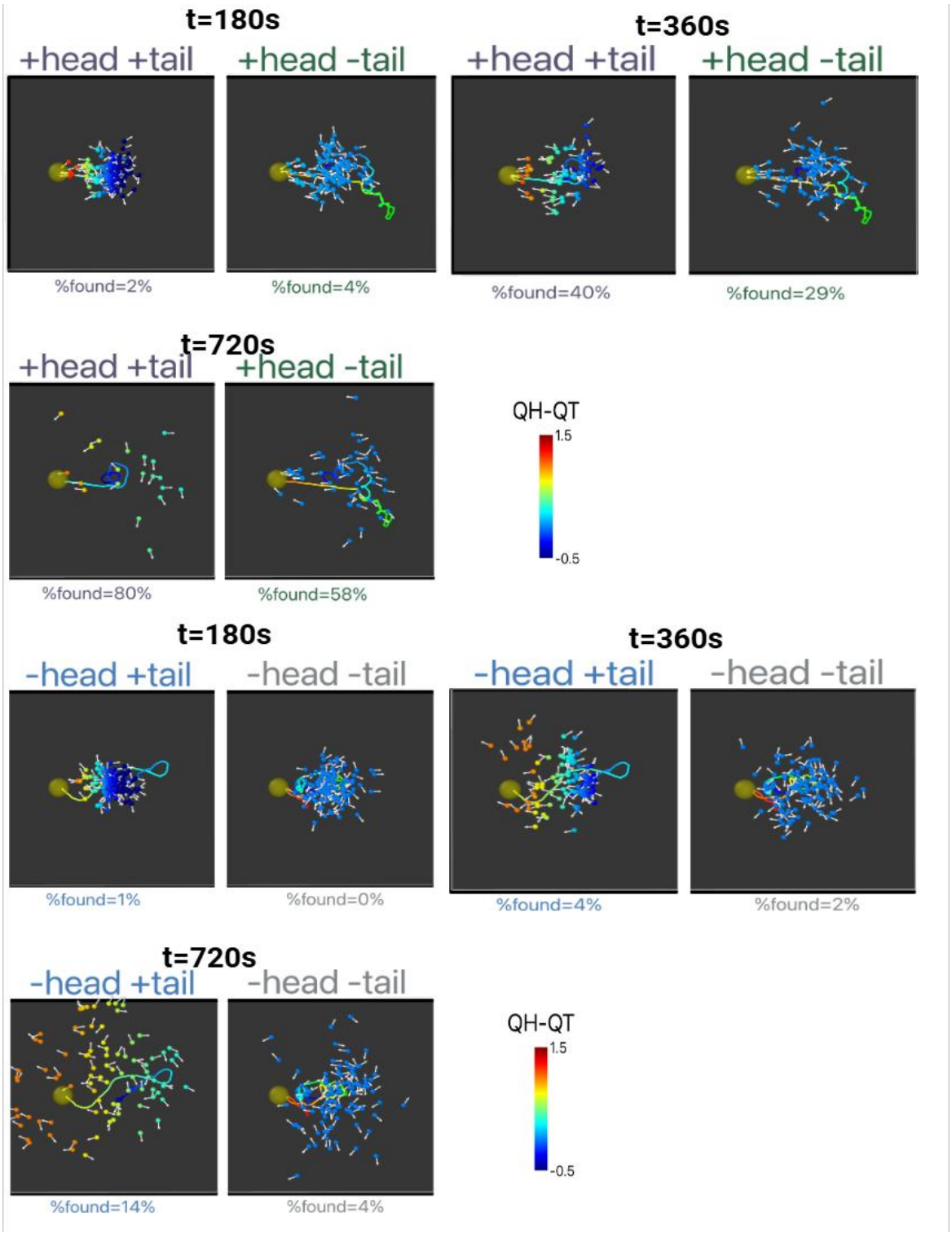

Figure S11: Each panel shows simulation snapshots comparing head/tail input-enabled conditions. In each snapshot with a time point, 100 randomly chosen worms from 10,000 stimulation events are displayed as spheres, colored by their instantaneous confidence $Q^H - Q^T$.

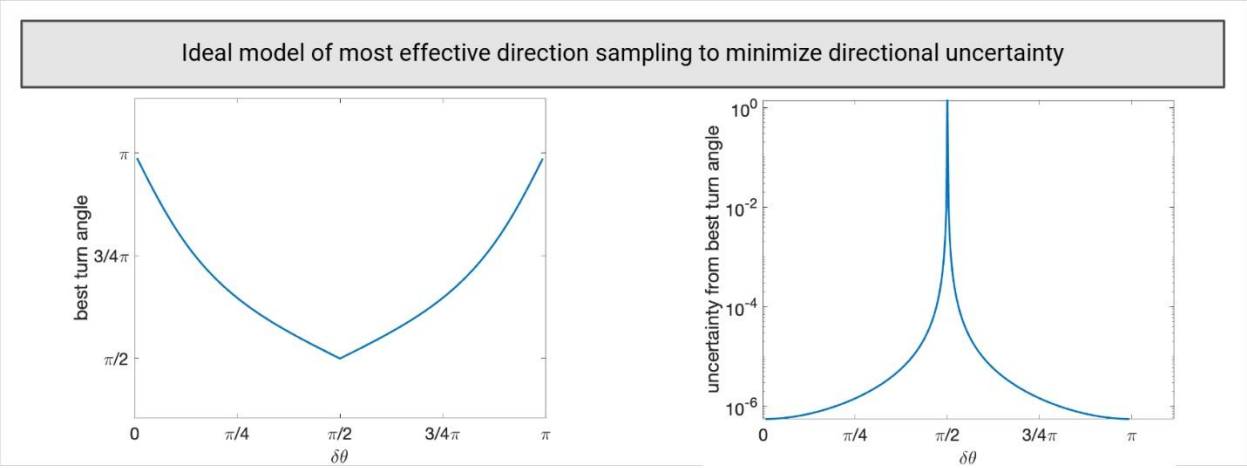

Figure S12: Ideal model for effective direction sampling to minimize directional uncertainty. δθ is the angle between the first sampled direction and the concentration gradient. The left panel shows the best angle to turn to sample the second direction. The right panel shows the directional uncertainty associated with the best turn angle. Averaging over an assumed uniform distribution of δθ results in a best turn angle close to 120 degrees.

Author contributions

X.W. and P.W.S. conceived the study and designed the experiments. X.W. and V.S. performed the behavioral assays, imaging, and optogenetics experiments. T.Z. and X.W. designed the computational model, performed the simulation and data analysis. X.W. and A.G. performed the microfluidics chip-based experiment. C.F.P. provided a whole-brain imaging data analysis platform. X.W., T.Z., and P.W.S. wrote the initial draft of the manuscript. All authors discussed the results and contributed to the final version of the manuscript. P.W.S., A.D.T.S., and P.W.S. supervised the project.

ACKNOWLEDGMENTS:

We are grateful to David Aguirre, Wilber Palma, Stephanie Nava, and Zachary Blumenfeld for their assistance during the early stages of this project. We acknowledge Natalie Sim and Elena Ruiz for data analysis. We also thank Helena Casademunt and Nicholas Markarian for their discussion and suggestions during the manuscript preparation. This work was supported by: R01 NS113119 (PWS, ADTS), Tianqiao and Chrissy Chen Institute for Neuroscience senior postdoc fellowship, Tianqiao and Chrissy Chen Institute for Neuroscience postdoc innovator grant and Tianqiao and Chrissy Chen Institute for Neuroscience Systems Neuroscience Awards. PWS is Bren Professor of Biology. The *Caenorhabditis* Genetics Center provided some strains.

DISCLOSURES:

The authors have no conflicts of interest to disclose.

Data availability

Source data are provided with this paper.

Code availability

All code for data analysis is available at https://github.com/edmondztt/pheromone-traj-analysis.

Reference list:

1 Simon, J. M. & Sternberg, P. W. Evidence of a mate-finding cue in the hermaphrodite nematode *Caenorhabditis elegans*. *Proceedings of the National Academy of Sciences* **99**, 1598-1603 (2002).

2 Lipton, J., Kleemann, G., Ghosh, R., Lints, R. & Emmons, S. W. Mate searching in *Caenorhabditis elegans*: a genetic model for sex drive in a simple invertebrate. *The Journal of neuroscience : the official journal of the Society for Neuroscience* **24**, 7427-7434, doi:10.1523/JNEUROSCI.1746-04.2004 [doi] (2004).

3 Leighton, D. H., Choe, A., Wu, S. Y. & Sternberg, P. W. Communication between oocytes and somatic cells regulates volatile pheromone production in *Caenorhabditis elegans*. *Proc Natl Acad Sci U S A* **111**, 17905-17910, doi:10.1073/pnas.1420439111 (2014).

4 Wan, X. *et al.* SRD-1 in AWA neurons is the receptor for female volatile sex pheromones in *C. elegans* males. *EMBO Rep* **20**, doi:10.15252/embr.201846288 (2019).

5 Chasnov, J. R., So, W. K., Chan, C. M. & Chow, K. L. The species, sex, and stage specificity of a *Caenorhabditis* sex pheromone. *Proc Natl Acad Sci U S A* **104**, 6730-6735, doi:10.1073/pnas.0608050104 (2007).

6 Lockery, S. R. The computational worm: spatial orientation and its neuronal basis in *C. elegans*. *Current opinion in neurobiology* **21**, 782-790 (2011).

7 Schone, H. *Spatial orientation: The spatial control of behavior in animals and man*. Vol. 588 (Princeton University Press, 2014).

8 Grasso, F. W. & Basil, J. A. How lobsters, crayfishes, and crabs locate sources of odor: current perspectives and future directions. *Current opinion in neurobiology* **12**, 721-727 (2002).

9 Gomez-Diaz, C. & Benton, R. The joy of sex pheromones. *EMBO reports* **14**, 874-883, doi:10.1038/embor.2013.140 [doi] (2013).

10 Moncho-Bogani, J., Lanuza, E., Lorente, M. J. & Martinez-Garcia, F. Attraction to male pheromones and sexual behaviour show different regulatory mechanisms in female mice. *Physiol Behav* **81**, 427-434, doi:10.1016/j.physbeh.2004.01.014 (2004).

11 Moncho-Bogani, J., Martinez-Garcia, F., Novejarque, A. & Lanuza, E. Attraction to sexual pheromones and associated odorants in female mice involves activation of the reward system and basolateral amygdala. *Eur J Neurosci* **21**, 2186-2198, doi:10.1111/j.1460-9568.2005.04036.x (2005).

12 Kurtovic, A., Widmer, A. & Dickson, B. J. A single class of olfactory neurons mediates behavioural responses to a *Drosophila* sex pheromone. *Nature* **446**, 542-546 (2007).

13 Stockinger, P., Kvitsiani, D., Rotkopf, S., Tirián, L. & Dickson, B. J. Neural circuitry that governs *Drosophila* male courtship behavior. *Cell* **121**, 795-807 (2005).

14 Datta, S. R. *et al.* The *Drosophila* pheromone cVA activates a sexually dimorphic neural circuit. *Nature* **452**, 473-477 (2008).

15 Miyamoto, T. & Amrein, H. Suppression of male courtship by a *Drosophila* pheromone receptor. *Nature neuroscience* **11**, 874-876 (2008).

16 Ruta, V. *et al.* A dimorphic pheromone circuit in *Drosophila* from sensory input to descending output. *Nature* **468**, 686-690 (2010).

17 Hofman, M. A. & Swaab, D. F. The sexually dimorphic nucleus of the preoptic area in the human brain: a comparative morphometric study. *Journal of anatomy* **164**, 55 (1989).

18 Wei, D., Talwar, V. & Lin, D. Neural circuits of social behaviors: Innate yet flexible. *Neuron* **109**, 1600-1620 (2021).

19 Auer, T. O. & Benton, R. Sexual circuitry in *Drosophila*. *Current opinion in neurobiology* **38**, 18-26 (2016).

1415 20 Yang, C. F. & Shah, N. M. Representing sex in the brain, one module at a time. *Neuron* **82**, 261-
1416 278 (2014).
1417 21 De Vries, G. J. & Simerly, R. B. in *Hormones, brain and behavior* 137-XXIX (Elsevier, 2002).
1418 22 Cachero, S., Ostrovsky, A. D., Jai, Y. Y., Dickson, B. J. & Jefferis, G. S. Sexual dimorphism in the fly
1419 brain. *Current biology* **20**, 1589-1601 (2010).
1420 23 Peckol, E. L., Troemel, E. R. & Bargmann, C. I. Sensory experience and sensory activity regulate
1421 chemosensory receptor gene expression in *Caenorhabditis elegans*. *Proceedings of the National*
1422 *Academy of Sciences of the United States of America* **98**, 11032-11038,
1423 doi:10.1073/pnas.191352498 [doi] (2001).
1424 24 Ludewig, A. H. *et al.* Pheromone sensing regulates *Caenorhabditis elegans* lifespan and stress
1425 resistance via the deacetylase SIR-2.1. *Proc Natl Acad Sci U S A* **110**, 5522-5527,
1426 doi:10.1073/pnas.1214467110 (2013).
1427 25 Golden, J. W. & Riddle, D. L. A pheromone influences larval development in the nematode
1428 *Caenorhabditis elegans*. *Science* **218**, 578-580, doi:10.1126/science.6896933 (1982).
1429 26 Butcher, R. A., Fujita, M., Schroeder, F. C. & Clardy, J. Small-molecule pheromones that control
1430 dauer development in *Caenorhabditis elegans*. *Nature chemical biology* **3**, 420-422 (2007).
1431 27 Jeong, P. Y. *et al.* Chemical structure and biological activity of the *Caenorhabditis elegans* dauer-
1432 inducing pheromone. *Nature* **433**, 541-545, doi:10.1038/nature03201 (2005).
1433 28 Butcher, R. A., Ragains, J. R., Kim, E. & Clardy, J. A potent dauer pheromone component in
1434 *Caenorhabditis elegans* that acts synergistically with other components. *Proc Natl Acad Sci U S A*
1435 **105**, 14288-14292, doi:10.1073/pnas.0806676105 (2008).
1436 29 Aprison, E. Z. & Ruvinsky, I. Counteracting Ascarosides Act through Distinct Neurons to
1437 Determine the Sexual Identity of *C. elegans* Pheromones. *Curr Biol* **27**, 2589-2599 e2583,
1438 doi:10.1016/j.cub.2017.07.034 (2017).
1439 30 Aprison, E. Z. & Ruvinsky, I. Sex Pheromones of *C. elegans* Males Prime the Female Reproductive
1440 System and Ameliorate the Effects of Heat Stress. *PLoS Genet* **11**, e1005729,
1441 doi:10.1371/journal.pgen.1005729 (2015).
1442 31 Kaplan, F. *et al.* Ascaroside expression in *Caenorhabditis elegans* is strongly dependent on diet
1443 and developmental stage. *PLoS One* **6**, e17804, doi:10.1371/journal.pone.0017804 (2011).
1444 32 Srinivasan, J. *et al.* A modular library of small molecule signals regulates social behaviors in
1445 *Caenorhabditis elegans*. *PLoS biology* **10**, e1001237 (2012).
1446 33 Srinivasan, J. *et al.* A blend of small molecules regulates both mating and development in
1447 *Caenorhabditis elegans*. *Nature* **454**, 1115-1118 (2008).
1448 34 Ludewig, A. H. & Schroeder, F. C. Ascaroside signaling in *C. elegans*. *WormBook*, 1-22,
1449 doi:10.1895/wormbook.1.155.1 (2013).
1450 35 Choe, A. *et al.* Ascaroside signaling is widely conserved among nematodes. *Curr Biol* **22**, 772-780,
1451 doi:10.1016/j.cub.2012.03.024 (2012).
1452 36 von Reuss, S. H. *et al.* Comparative metabolomics reveals biogenesis of ascarosides, a modular
1453 library of small-molecule signals in *C. elegans*. *J Am Chem Soc* **134**, 1817-1824,
1454 doi:10.1021/ja210202y (2012).
1455 37 Choe, A. *et al.* Sex-specific mating pheromones in the nematode Panagrellus redivivus. *Proc Natl*
1456 *Acad Sci U S A* **109**, 20949-20954, doi:10.1073/pnas.1218302109 (2012).
1457 38 Hsueh, Y. P., Mahanti, P., Schroeder, F. C. & Sternberg, P. W. Nematode-trapping fungi eavesdrop
1458 on nematode pheromones. *Curr Biol* **23**, 83-86, doi:10.1016/j.cub.2012.11.035 (2013).
1459 39 Pungaliya, C. *et al.* A shortcut to identifying small molecule signals that regulate behavior and
1460 development in *Caenorhabditis elegans*. *Proc Natl Acad Sci U S A* **106**, 7708-7713,
1461 doi:10.1073/pnas.0811918106 (2009).

40 Izrayelit, Y. *et al.* Targeted metabolomics reveals a male pheromone and sex-specific ascaroside biosynthesis in *Caenorhabditis elegans*. *ACS chemical biology* **7**, 1321-1325 (2012).
41 Fagan, K. A. *et al.* A Single-Neuron Chemosensory Switch Determines the Valence of a Sexually Dimorphic Sensory Behavior. *Curr Biol* **28**, 902-914 e905, doi:10.1016/j.cub.2018.02.029 (2018).
42 Chasnov, J. R., So, W. K., Chan, C. M. & Chow, K. L. The species, sex, and stage specificity of a *Caenorhabditis* sex pheromone. *Proceedings of the National Academy of Sciences of the United States of America* **104**, 6730-6735, doi:0608050104 [pii] (2007).
43 Kato, S., Xu, Y., Cho, C. E., Abbott, L. & Bargmann, C. I. Temporal responses of *C. elegans* chemosensory neurons are preserved in behavioral dynamics. *Neuron* **81**, 616-628 (2014).
44 Luo, L. *et al.* Dynamic encoding of perception, memory, and movement in a *C. elegans* chemotaxis circuit. *Neuron* **82**, 1115-1128 (2014).
45 Wang, L. *et al.* A gustatory neural circuit of *Caenorhabditis elegans* generates memory-dependent behaviors in Na+ chemotaxis. *Journal of Neuroscience* **37**, 2097-2111 (2017).
46 Satoh, Y. *et al.* Regulation of experience-dependent bidirectional chemotaxis by a neural circuit switch in *Caenorhabditis elegans*. *Journal of Neuroscience* **34**, 15631-15637 (2014).
47 Kunitomo, H. *et al.* Concentration memory-dependent synaptic plasticity of a taste circuit regulates salt concentration chemotaxis in *Caenorhabditis elegans*. *Nature communications* **4**, 2210 (2013).
48 Ji, N. *et al.* Corollary discharge promotes a sustained motor state in a neural circuit for navigation. *Elife* **10**, e68848 (2021).
49 Venkatachalam, V. *et al.* Pan-neuronal imaging in roaming *Caenorhabditis elegans*. *Proceedings of the National Academy of Sciences* **113**, E1082-E1088 (2016).
50 Zhen, M. & Samuel, A. D. *C. elegans* locomotion: small circuits, complex functions. *Current opinion in neurobiology* **33**, 117-126 (2015).
51 Chalasani, S. H. *et al.* Dissecting a circuit for olfactory behaviour in *Caenorhabditis elegans*. *Nature* **450**, 63-70 (2007).
52 Gray, J. M., Hill, J. J. & Bargmann, C. I. A circuit for navigation in *Caenorhabditis elegans*. *Proceedings of the National Academy of Sciences* **102**, 3184-3191 (2005).
53 Larsch, J. *et al.* A circuit for gradient climbing in *C. elegans* chemotaxis. *Cell reports* **12**, 1748-1760 (2015).
54 Dobosiewicz, M., Liu, Q. & Bargmann, C. I. Reliability of an interneuron response depends on an integrated sensory state. *Elife* **8**, e50566 (2019).
55 Luo, L. *et al.* Bidirectional thermotaxis in *Caenorhabditis elegans* is mediated by distinct sensorimotor strategies driven by the AFD thermosensory neurons. *Proceedings of the National Academy of Sciences* **111**, 2776-2781 (2014).
56 Colbert, H. A. & Bargmann, C. I. Environmental signals modulate olfactory acuity, discrimination, and memory in *Caenorhabditis elegans*. *Learning & memory (Cold Spring Harbor, N.Y.)* **4**, 179-191 (1997).
57 Wen, J. Y. M. *et al.* Mutations that prevent associative learning in *C. elegans*. *Behavioral neuroscience* **111**, 354 (1997).
58 Saeki, S., Yamamoto, M. & Iino, Y. Plasticity of chemotaxis revealed by paired presentation of a chemoattractant and starvation in the nematode *Caenorhabditis elegans*. *The Journal of experimental biology* **204**, 1757-1764 (2001).
59 Nuttley, W. M., Atkinson-Leadbeater, K. P. & Van Der Kooy, D. Serotonin mediates food-odor associative learning in the nematode *Caenorhabditis*elegans. *Proceedings of the National Academy of Sciences of the United States of America* **99**, 12449-12454, doi:10.1073/pnas.192101699 [doi] (2002).

60 Zhang, Y., Lu, H. & Bargmann, C. I. Pathogenic bacteria induce aversive olfactory learning in *Caenorhabditis elegans*. *Nature* **438**, 179-184 (2005).
61 Vellai, T., McCulloch, D., Gems, D. & Kovács, A. L. Effects of sex and insulin/insulin-like growth factor-1 signaling on performance in an associative learning paradigm in *Caenorhabditis elegans*. *Genetics* **174**, 309-316 (2006).
62 Kauffman, A. *et al. C. elegans* positive butanone learning, short-term, and long-term associative memory assays. *J Vis Exp*, doi:10.3791/2490 (2011).
63 Sakai, N. *et al.* A sexually conditioned switch of chemosensory behavior in *C. elegans*. *PLoS One* **8**, e68676, doi:10.1371/journal.pone.0068676 (2013).
64 Stein, G. M. & Murphy, C. T. *C. elegans* positive olfactory associative memory is a molecularly conserved behavioral paradigm. *Neurobiol Learn Mem* **115**, 86-94, doi:10.1016/j.nlm.2014.07.011 (2014).
65 Hong, M. *et al.* Early Pheromone Experience Modifies a Synaptic Activity to Influence Adult Pheromone Responses of *C. elegans*. *Curr Biol* **27**, 3168-3177 e3163, doi:10.1016/j.cub.2017.08.068 (2017).
66 Gordus, A., Pokala, N., Levy, S., Flavell, S. W. & Bargmann, C. I. Feedback from network states generates variability in a probabilistic olfactory circuit. *Cell* **161**, 215-227 (2015).
67 Hilliard, M. A., Bargmann, C. I. & Bazzicalupo, P. *C. elegans* responds to chemical repellents by integrating sensory inputs from the head and the tail. *Current Biology* **12**, 730-734 (2002).
68 Gat, A. *et al.* Integration of spatially opposing cues by a single interneuron guides decision making in *C. elegans*. *bioRxiv*, 2023.2001. 2023.525194 (2023).
69 Quintin, S., Aspert, T., Ye, T. & Charvin, G. Distinct mechanisms underlie H2O2 sensing in *C. elegans* head and tail. *Plos one* **17**, e0274226 (2022).
70 Troemel, E. R., Chou, J. H., Dwyer, N. D., Colbert, H. A. & Bargmann, C. I. Divergent seven transmembrane receptors are candidate chemosensory receptors in *C. elegans*. *Cell* **83**, 207-218 (1995).
71 Yi, W., Ross, J. M. & Zarkower, D. Mab-3 is a direct tra-1 target gene regulating diverse aspects of *C. elegans* male sexual development and behavior. *Development* **127**, 4469-4480 (2000).
72 Molina-García, L. *et al.* Direct glia-to-neuron transdifferentiation gives rise to a pair of male-specific neurons that ensure nimble male mating. *Elife* **9**, e48361 (2020).
73 Morillo, K. S., St. Ange, J., Weng, Y., Kaletsky, R. & Murphy, C. T. Single-Nucleus Neuronal Transcriptional Profiling of Male *C. elegans* Uncovers Regulators of Sex-Specific and Sex-Shared Behaviors. *bioRxiv*, 2024.2012. 2012.628226 (2024).
74 Susoy, V. *et al.* Natural sensory context drives diverse brain-wide activity during *C. elegans* mating. *Cell* **184**, 5122-5137. e5117 (2021).
75 Sengupta, P., Chou, J. H. & Bargmann, C. I. odr-10 encodes a seven transmembrane domain olfactory receptor required for responses to the odorant diacetyl. *Cell* **84**, 899-909, doi:10.1016/s0092-8674(00)81068-5 (1996).
76 Bargmann, C. I. Chemosensation in *C. elegans*. *WormBook : the online review of C.elegans biology*, 1-29, doi:10.1895/wormbook.1.123.1 [doi] (2006).
77 Ferkey, D. M., Sengupta, P. & L'Etoile, N. D. Chemosensory signal transduction in *Caenorhabditis elegans*. *Genetics* **217**, iyab004 (2021).
78 Im Choi, J. *et al.* Odor-dependent temporal dynamics in Caenorhabitis elegans adaptation and aversive learning behavior. *PeerJ* **6**, e4956 (2018).
79 Bargmann, C. I., Hartwieg, E. & Horvitz, H. R. Odorant-selective genes and neurons mediate olfaction in *C. elegans*. *Cell* **74**, 515-527 (1993).
80 Tran, A. *et al. C. elegans* avoids toxin-producing Streptomyces using a seven transmembrane domain chemosensory receptor. *Elife* **6**, e23770 (2017).

81 Zhou, Y. *et al.* Potential Nematode Alarm Pheromone Induces Acute Avoidance in *Caenorhabditis elegans*. *Genetics* **206**, 1469-1478, doi:10.1534/genetics.116.197293 (2017).
82 Klapoetke, N. C. *et al.* Independent optical excitation of distinct neural populations. *Nature methods* **11**, 338-346 (2014).
83 Cook, S. J. *et al.* Whole-animal connectomes of both *Caenorhabditis elegans* sexes. *Nature* **571**, 63-71 (2019).
84 Cohen, N. & Denham, J. E. Whole animal modeling: piecing together nematode locomotion. *Current Opinion in Systems Biology* **13**, 150-160 (2019).
85 Kato, S. *et al.* Global brain dynamics embed the motor command sequence of *Caenorhabditis elegans*. *Cell* **163**, 656-669 (2015).
86 Meng, J. *et al.* A tonically active master neuron modulates mutually exclusive motor states at two timescales. (2023).
87 Choi, M.-K., Liu, H., Wu, T., Yang, W. & Zhang, Y. NMDAR-mediated modulation of gap junction circuit regulates olfactory learning in *C. elegans*. *Nature Communications* **11**, 3467 (2020).
88 Marvin, J. S. *et al.* An optimized fluorescent probe for visualizing glutamate neurotransmission. *Nature methods* **10**, 162-170 (2013).
89 Albrecht, D. R. & Bargmann, C. I. High-content behavioral analysis of *Caenorhabditis elegans* in precise spatiotemporal chemical environments. *Nature methods* **8**, 599-605 (2011).
90 Cheung, B. H., Cohen, M., Rogers, C., Albayram, O. & De Bono, M. Experience-dependent modulation of *C. elegans* behavior by ambient oxygen. *Current Biology* **15**, 905-917 (2005).
91 Bretscher, A. J. *et al.* Temperature, oxygen, and salt-sensing neurons in *C. elegans* are carbon dioxide sensors that control avoidance behavior. *Neuron* **69**, 1099-1113, doi:10.1016/j.neuron.2011.02.023 (2011).
92 Ryu, W. S. & Samuel, A. D. Thermotaxis in *Caenorhabditis elegans* analyzed by measuring responses to defined thermal stimuli. *Journal of Neuroscience* **22**, 5727-5733 (2002).
93 Gabel, C. V. *et al.* Neural circuits mediate electrosensory behavior in *Caenorhabditis elegans*. *Journal of Neuroscience* **27**, 7586-7596 (2007).
94 Sawin, E. R., Ranganathan, R. & Horvitz, H. R. *C. elegans* locomotory rate is modulated by the environment through a dopaminergic pathway and by experience through a serotonergic pathway. *Neuron* **26**, 619-631 (2000).
95 Pierce-Shimomura, J. T., Morse, T. M. & Lockery, S. R. The fundamental role of pirouettes in *Caenorhabditis elegans* chemotaxis. *Journal of Neuroscience* **19**, 9557-9569 (1999).
96 Iino, Y. & Yoshida, K. Parallel use of two behavioral mechanisms for chemotaxis in *Caenorhabditis elegans*. *Journal of Neuroscience* **29**, 5370-5380 (2009).
97 Miller, A. C., Thiele, T. R., Faumont, S., Moravec, M. L. & Lockery, S. R. Step-response analysis of chemotaxis in *Caenorhabditis elegans*. *Journal of Neuroscience* **25**, 3369-3378 (2005).
98 Zariwala, H. A., Miller, A. C., Faumont, S. & Lockery, S. R. Step response analysis of thermotaxis in *Caenorhabditis elegans*. *Journal of Neuroscience* **23**, 4369-4377 (2003).
99 Schimansky-Geier, L., Mieth, M., Rosé, H. & Malchow, H. Structure formation by active Brownian particles. *Physics Letters A* **207**, 140-146 (1995).
100 Berg, H. C. *E. coli in Motion*. (Springer, 2004).
101 Ibarra-Soria, X., Levitin, M. O., Saraiva, L. R. & Logan, D. W. The olfactory transcriptomes of mice. *PLoS genetics* **10**, e1004593 (2014).
102 Kohl, J., Ostrovsky, A. D., Frechter, S. & Jefferis, G. S. A bidirectional circuit switch reroutes pheromone signals in male and female brains. *Cell* **155**, 1610-1623 (2013).
103 Gat, A. *et al.* Integration of spatially opposing cues by a single interneuron guides decision-making in *C. elegans*. *Cell Reports* **42** (2023).

104 Page, J. L., Dickman, B. D., Webster, D. R. & Weissburg, M. J. Staying the course: chemical signal spatial properties and concentration mediate cross-stream motion in turbulent plumes. *Journal of Experimental Biology* **214**, 1513-1522 (2011).
105 Gomez-Marin, A., Duistermars, B., Frye, M. A. & Louis, M. Mechanisms of odor-tracking: multiple sensors for enhanced perception and behavior. *Frontiers in cellular neuroscience* **4**, 1374 (2010).
106 Borst, A. & Heisenberg, M. Osmotropotaxis in *Drosophila* melanogaster. *Journal of comparative physiology* **147**, 479-484 (1982).
107 Budick, S. A. & Dickinson, M. H. Free-flight responses of *Drosophila* melanogaster to attractive odors. *Journal of experimental biology* **209**, 3001-3017 (2006).
108 Taylor, S. R. *et al.* Molecular topography of an entire nervous system. *Cell* **184**, 4329-4347.e4323, doi:10.1016/j.cell.2021.06.023 (2021).
109 Yemini, E. *et al.* NeuroPAL: a multicolor atlas for whole-brain neuronal identification in *C. elegans*. *Cell* **184**, 272-288. e211 (2021).
110 Vidal, B. *et al.* An atlas of *Caenorhabditis elegans* chemoreceptor expression. *PLoS Biol* **16**, e2004218, doi:10.1371/journal.pbio.2004218 (2018).
111 Pereira, L. *et al.* Timing mechanism of sexually dimorphic nervous system differentiation. *Elife* **8**, doi:10.7554/eLife.42078 (2019).
112 Schindelin, J. *et al.* Fiji: an open-source platform for biological-image analysis. *Nature methods* **9**, 676-682 (2012).
113 Wolff, C. *et al.* Multi-view light-sheet imaging and tracking with the MaMuT software reveals the cell lineage of a direct developing arthropod limb. *Elife* **7**, e34410 (2018).
114 Park, C. F. *et al.* Automated neuron tracking inside moving and deforming *C. elegans* using deep learning and targeted augmentation. *Nature Methods* **21**, 142-149 (2024).
115 Berg, S. *et al.* Ilastik: interactive machine learning for (bio) image analysis. *Nature methods* **16**, 1226-1232 (2019).
116 Nava, S. *et al.* A cGAL-UAS bipartite expression toolkit for *Caenorhabditis elegans* sensory neurons. *Proceedings of the National Academy of Sciences* **120**, e2221680120 (2023).
117 Pokala, N., Liu, Q., Gordus, A. & Bargmann, C. I. Inducible and titratable silencing of *Caenorhabditis elegans* neurons in vivo with histamine-gated chloride channels. *Proc Natl Acad Sci U S A* **111**, 2770-2775, doi:10.1073/pnas.1400615111 (2014).
118 Cao, M., Chai, C., Liu, J. & Sternberg, P. Application of the red-shifted channel rhodopsin Chrimson for the *Caenorhabditis elegans* cGAL bipartite system. *MicroPubl Biol* **2018**, doi:10.17912/2jgw-fj52 (2018).
119 Schild, L. C. & Glauser, D. A. Dual color neural activation and behavior control with chrimson and CoChR in *Caenorhabditis elegans*. *Genetics* **200**, 1029-1034 (2015).
120 Lu, Y. *et al.* Extrasynaptic signaling enables an asymmetric juvenile motor circuit to produce symmetric undulation. *Current Biology* **32**, 4631-4644. e4635 (2022).
121 Gower, J. C. Generalized procrustes analysis. *Psychometrika* **40**, 33-51 (1975).
122 Wood, S. N. Thin plate regression splines. *Journal of the Royal Statistical Society Series B: Statistical Methodology* **65**, 95-114 (2003).
123 Zhou, T. *et al.* AI-aided geometric design of anti-infection catheters. *Science Advances* **10**, eadj1741 (2024).
124 Chronis, N., Zimmer, M. & Bargmann, C. I. Microfluidics for in vivo imaging of neuronal and behavioral activity in *Caenorhabditis elegans*. *Nature methods* **4**, 727-731 (2007).
125 Pinkard, H. *et al.* Pycro-Manager: open-source software for customized and reproducible microscope control. *Nature methods* **18**, 226-228 (2021).

126 Appleby, P. A. The role of multiple chemotactic mechanisms in a model of chemotaxis in *C. elegans*: different mechanisms are specialised for different environments. *Journal of computational neuroscience* **36**, 339-354 (2014).